

BEAMFORMING TECHNIQUES AND INTERFERENCE
MITIGATION USING A MULTIPLE FEED ARRAY FOR RADIO
ASTRONOMY

by

Chad K. Hansen

A thesis submitted to the faculty of

Brigham Young University

in partial fulfillment of the requirements for the degree of

Master of Science

Department of Electrical and Computer Engineering

Brigham Young University

April 2004

Copyright © 2004 Chad K. Hansen

All Rights Reserved

BRIGHAM YOUNG UNIVERSITY

GRADUATE COMMITTEE APPROVAL

of a thesis submitted by

Chad K. Hansen

This thesis has been read by each member of the following graduate committee and by majority vote has been found to be satisfactory.

Date

Dr. Karl F. Warnick, Chair

Date

Dr. Brian D. Jeffs

Date

Dr. Michael A. Jensen

BRIGHAM YOUNG UNIVERSITY

As chair of the candidate's graduate committee, I have read the thesis of Chad K. Hansen in its final form and have found that (1) its format, citations, and bibliographical style are consistent and acceptable and fulfill university and department style requirements; (2) its illustrative materials including figures, tables, and charts are in place; and (3) the final manuscript is satisfactory to the graduate committee and is ready for submission to the university library.

Date

Dr. Karl F. Warnick
Chair, Graduate Committee

Accepted for the Department

Dr. Michael A. Jensen
Graduate Coordinator

Accepted for the College

Dr. Douglas M. Chabries
Dean, College of Engineering and Technology

ABSTRACT

BEAMFORMING TECHNIQUES AND INTERFERENCE MITIGATION USING A MULTIPLE FEED ARRAY FOR RADIO ASTRONOMY

Chad K. Hansen

Department of Electrical and Computer Engineering

Master of Science

Radio frequency interference has become a large problem to radio astronomers. This thesis proposes the idea that radio frequency interference can be mitigated using a phased array feed in conjunction with a large reflector. A phased array feed would allow radio astronomers to observe fainter signals than is currently possible, while at the same time enabling rapid sky surveys. A phased array feed was designed and simulated, and sensitivity optimization was performed on the array feed. It was shown that higher sensitivity can be achieved using a 7-element phased array feed than with a conventional waveguide feed. Simulations were ran using RFI mitigation algorithms on the array to show that interference cancellation can, in principle, be performed using a phased array feed. In addition to these simulations, improvements were made to a previously designed RF receiver so that radio astronomy observations could be made and interference mitigation algorithms tested on a receiver platform.

ACKNOWLEDGMENTS

I would like to express appreciation to my academic advisor, Dr. Karl Warnick, for his guidance in my research and help in writing this thesis. I would also like to thank Dr. Brian Jeffs and Dr. Michael Jensen for their counsel and advice. I also appreciate the expertise Rick Fischer has contributed to my research. Thanks also goes to Brett Walkenhorst and Andy Poulsen for their help and support. Thanks also to the National Science Foundation for funding this research. And finally I want to thank my parents, Kurt and Vicky Hansen, for always believing in my potential and giving me the support I needed.

Contents

| | |
|--|--------------|
| Acknowledgments | xi |
| List of Tables | xv |
| List of Figures | xviii |
| 1 Introduction | 1 |
| 1.1 RFI Mitigation in Radio Astronomy | 1 |
| 1.2 Thesis Contributions | 3 |
| 1.3 Thesis Outline | 4 |
| 2 Background | 5 |
| 2.1 Radio Telescope VSA Receiver | 5 |
| 2.2 RF Receiver | 7 |
| 2.3 Sensitivity | 9 |
| 2.4 Multiple Feed Arrays in Radio Astronomy | 11 |
| 3 Receiver Improvements and VSA Observations | 15 |
| 3.1 RF Receiver Improvements | 15 |
| 3.2 VSA Observations | 19 |
| 4 Sensitivity Optimization with Multiple Feed Array | 25 |
| 4.1 Simulation Parameters | 25 |
| 4.2 Phased Array Feed Gain | 26 |
| 4.3 Spillover Efficiency | 27 |
| 4.4 Antenna Parameters | 28 |

| | | |
|----------|--|-----------|
| 4.5 | Waveguide Standard | 30 |
| 4.6 | Beamforming | 33 |
| 4.7 | Sensitivity Optimization | 34 |
| 4.8 | Beamscanning | 36 |
| 5 | RFI Mitigation using Phased Array Feed | 47 |
| 5.1 | Maximum SNR and LCMV | 47 |
| 5.2 | Maximum SNR Using 19-element Array | 56 |
| 5.3 | Analysis of SNR Behavior | 57 |
| 6 | Conclusion | 67 |
| 6.1 | Contributions | 67 |
| 6.2 | Future Work | 68 |
| A | Single Feed Gain Pattern Computation Using GRASP8 | 71 |
| B | Spillover Noise Model | 73 |
| | Bibliography | 77 |

List of Tables

| | | |
|-----|--------------------------------------|----|
| 2.1 | VSA antenna specifications | 6 |
| 3.1 | RF receiver specifications | 18 |
| 4.1 | VLA antenna specifications | 29 |

List of Figures

| | | |
|------|---|----|
| 2.1 | The BYU Very Small Array (VSA). | 6 |
| 2.2 | Block diagram of the radio telescope VSA receiver | 8 |
| 2.3 | Picture of original RF receiver | 8 |
| 2.4 | Electric fields in microstrip and coplanar waveguide | 10 |
| 2.5 | Parkes waveguide array feed | 12 |
| 2.6 | 19-element array feed at NRAO | 14 |
| 3.1 | Frequency response bandpass filter | 16 |
| 3.2 | Antenna positioning hardware, RF receiver system, real-time DSP platform, and BYU VSA control/receiver station | 18 |
| 3.3 | Glonass frequency spectrum | 20 |
| 3.4 | Cygnus and Casseiofia frequency spectrum with baseline | 21 |
| 3.5 | Cygnus and Casseiofia frequency spectrum without baseline | 22 |
| 3.6 | VSA cancellation of an FM sweep signal in the presence of the Cygnus 1420 MHz hydrogen line | 24 |
| 4.1 | Spillover noise for an array feed | 27 |
| 4.2 | Reflector antenna used in simulations | 30 |
| 4.3 | Hexagonal array feed | 31 |
| 4.4 | Sensitivity vs. diameter for a circular waveguide feed | 31 |
| 4.5 | Gain vs. diameter for a circular waveguide feed | 32 |
| 4.6 | Spillover efficiency vs. diameter for a circular waveguide feed | 32 |
| 4.7 | Sampling of the beam pattern of a reflector dish with a waveguide feed | 33 |
| 4.8 | Beamformer for a reflector antenna with a phased array feed | 35 |
| 4.9 | Sensitivity vs. feed displacement | 37 |
| 4.10 | Gain vs. feed displacement | 37 |

| | |
|---|----|
| 4.11 Spillover efficiency vs. feed displacement | 38 |
| 4.12 Optimized array pattern on reflector dish | 38 |
| 4.13 Beam scanning with a reflector antenna | 39 |
| 4.14 Sensitivity vs. steered beam angle | 40 |
| 4.15 Gain vs. steered beam angle | 41 |
| 4.16 Spillover efficiency vs. steered beam angle | 41 |
| 4.17 Focal field distribution of plane wave on reflector dish | 43 |
| 4.18 ϕ -cut of beam patterns of 6 outer beams | 44 |
| 4.19 θ -cut of beam patterns of 7 beams | 44 |
| 4.20 Sensitivity of 7 beams | 45 |
| 5.1 Beam pattern using max SNR | 51 |
| 5.2 Detail of beam pattern null using max SNR | 51 |
| 5.3 Effective sensitivity vs. INR _{in} using max SNR | 52 |
| 5.4 Max SNR distorted beam pattern | 53 |
| 5.5 Effective sensitivity vs. interferer arrival angle using max SNR | 54 |
| 5.6 Max SNR and optimum sensitivity vs. interferer arrival angle | 54 |
| 5.7 Effective sensitivity compared to basic sensitivity | 55 |
| 5.8 Interference rejection vs. interferer location | 55 |
| 5.9 Effective sensitivity vs. interferer arrival angle for 19-element array feed using max SNR | 57 |
| 5.10 INR _{IN} vs. interferer location | 58 |
| 5.11 Gain vs. interferer arrival angle using max SNR | 59 |
| 5.12 Spillover efficiency vs. interferer arrival angle using max SNR | 59 |
| 5.13 Drop in SNR vs. interferer location | 63 |
| 5.14 $\mathbf{v}_L^H \mathbf{d}_i$ in SNR vs. interferer location | 64 |
| 5.15 Comparison between \mathbf{d}_s and \mathbf{d}_i | 64 |
| 5.16 Effective sensitivity vs. amplitudes of outer element weights | 65 |
| B.1 Two dimensional spillover noise model | 74 |
| B.2 Spillover noise model for array feed | 76 |

Chapter 1

Introduction

1.1 RFI Mitigation in Radio Astronomy

For centuries people have studied the stars trying to learn more about the universe we live in. Until Karl Jansky discovered radio emissions from the Milky Way in 1933, this was done using only optical telescopes. Since that time scientists have studied objects and phenomena in the universe using radio waves. Radio astronomy allows the study of some phenomena not available to traditional astronomers such as the cosmic background radiation.

Radio astronomy is the study of radio frequency emissions between a few kHz and approximately 300 GHz. A major problem in radio astronomy is that wireless communications use frequencies within this band. Many of the signals astronomers are trying to observe are very small, usually below the noise floor requiring long observation times. Because of this, even small power levels from satellites or other transmitting devices cause the bands to be corrupted and unobservable. This corruption from communication devices is known as radio frequency interference (RFI).

Over the years a great deal of work has been devoted to minimizing the interference. In the United States the Federal Communications Commission (FCC) has allocated many frequency bands for radio astronomy use, as have other agencies such as the International Telecommunications Union (ITU). Some areas in the United States have been designated radio free quiet zones. Some countries have not followed these guidelines. Another problem is that radio astronomers would like to study other important astronomical signals that are outside of protected bands. Ground based

uplink stations and radar cause a large portion of this interference, but the major problem of radio frequency interference comes from communication satellite downlinks. One major source of interference comes from the Russian Federation Global Navigation Satellite System (GLONASS). The GLONASS signal overlaps a very important frequency of interest, 1612 MHz, the spectral emission of Hydroxyl (OH) ions. This particular satellite system is the Russian equivalent of the United States' Global Positional System (GPS). It is difficult to find any observation area that will not be affected by the satellite system. These satellites emit high power signals, making it very difficult to see faint sources, even when the satellite signals are only seen in the deep sidelobes of radio telescopes.

Many large radio astronomy observatories are researching new methods to eliminate radio frequency interference. The National Radio Astronomy Observatory (NRAO) has been heavily involved in RFI mitigation. A real-time adaptive canceller using hardware [1] was built and NRAO has researched various techniques used in dealing with interference such as blanking and spatial nulling [2], [3]. The NRAO has also done work attenuating RFI by using imaging arrays [4]. RFI mitigation research is also being done at the Australia Telescope National Facility (ATNF) and the Netherlands Foundation for Research in Astronomy (NFRA) [5]. The ATNF has collaborated with Ohio State University to successfully eliminate a GLONASS interferer using parametric signal modelling and subtractions [6]. Two other radio astronomy observatories that are still under design and construction are also considering methods of RFI mitigation. These include the Allen Telescope Array (ATA) and the Square Kilometer Array (SKA) [7], [8].

The BYU radio astronomy research group is also involved in various methods of RFI mitigation. The performance of adaptive algorithms have been tested with respect to satellite interference cancellation [9]. A study of the use of an auxiliary antenna has been performed on radio astronomy imaging arrays [10], [11]. A great deal of work has also been done using an adaptive real-time least-mean square (LMS) algorithm to cancel satellite interference [12], [13]. Using this last method, the BYU research group performed a successful interference mitigation test on the Green Bank

Telescope (GBT) at NRAO. Another research area is the use of a Kalman tracker to perform time blanking of an air traffic control radar interference at NRAO.

1.2 Thesis Contributions

The main contribution of this thesis is the simulation of a phased array feed for use in radio astronomy and RFI mitigation. The phased array feed is shown to have a higher sensitivity than a conventional waveguide feed. This would enable astronomers to observe fainter signals in a shorter time. The phased array feed also has beamsteering capabilities, allowing radio astronomers to steer the main beam electronically without having to physically move the reflector. With beamsteering, the formation of multiple beams is possible. These beams can be formed electronically and used to rapidly survey the sky. Rapid sky surveys can significantly reduce observation times and can eliminate the need to move the reflector antenna as often during sky surveys. An analysis is also performed on arrays placed in different vertical planes and it is shown that a focal plane array produces the highest sensitivity.

Additionally, a phased array feed has the ability to perform RFI mitigation. This approach has not been attempted before in radio astronomy. It is shown that a 7-element phased array feed can effectively eliminate a satellite interferer while still maintaining high sensitivity. The phased array can cancel interferers with low and high power levels. An analysis of some of the limitations of the array is performed. For example, at some interference arrival angles the sensitivity of the array feed drops. A 19-element array feed is also simulated and compared to the 7-element array. The 19-element array is able to produce a higher sensitivity than the 7-element array and is more stable with different interference arrival angles.

Another contribution is the improvements made to a previously designed RF receiver. These improvements significantly reduced the noise entering the receiver and made it possible for radio astronomy observations to be made using the BYU Very Small Array (VSA) receivers. This also allowed interference mitigation algorithms to be implemented and tested on the VSA platform.

1.3 Thesis Outline

This thesis is organized as follows:

Chapter 2, *Background*, provides details of the VSA platform including the RF receiver. It defines sensitivity and its components. It also describes past and current research in using multiple feed arrays for use in radio astronomy.

Chapter 3, *Receiver Improvements and VSA Observations*, provides details on the improvements made to the VSA RF receiver and observations made with the receiver.

Chapter 4, *Sensitivity Optimization with Multiple Feed Array*, provides a background on sensitivity used in radio astronomy. It describes the process of optimizing sensitivity on a multiple feed array in conjunction with a reflector dish antenna. It provides examples of sensitivity optimizations and beamscanning capabilities of the array.

Chapter 5, *RFI Mitigation using Phased Array Feed*, describes two algorithms used in RFI mitigation and provides implementations of these algorithms on a phased array feed. Examples and details of interference mitigation are given.

Chapter 6, *Conclusion*, provides a summary of the contributions of this thesis to the BYU Research group and the radio astronomy community. It also lists directions for possible future work.

Appendix A, *Single Feed Gain Pattern Computation Using GRASP8*, provides details on how gain patterns of phased array elements are obtained using GRASP8 reflector antenna analysis software.

Appendix B, *Spillover Noise Model*, outlines the procedure for finding the correlation between antenna array elements due to spillover noise.

Chapter 2

Background

This chapter provides details on the VSA receiver system. It describes all of the components of the system including the RF receiver. The chapter outlines the components of the RF receiver system and their purpose. It defines sensitivity and its components. A background is also provided on multiple feed arrays and their use in radio astronomy.

2.1 Radio Telescope VSA Receiver

The BYU research group needed a way to test RFI mitigation algorithms. Results can be obtained using computer simulations and synthesized data, but it is difficult to model all of the real world parameters involved in a radio astronomy observation. The BYU Very Small Array (VSA) was developed for this purpose. This test platform enabled us to perform real-time observations and tests.

The VSA telescope receivers include dish antennas, positioning and tracking software, a low-noise RF receiver, and a 4-channel DSP. The VSA antennas and positioning hardware are the same as the Small Radio Telescope (SRT) developed by MIT's Haystack Observatory [14]. The SRT was developed primarily for educational purposes. The three antennas are manufactured by Kaul-Tronics, Inc. and their specifications can be seen in Table 2.1. They are inexpensive 10-foot diameter parabolic dish antennas made of aluminum. Each antenna is steered using a dual azimuth/elevation motor. Although most radio telescopes are much larger and of higher quality, the VSA antennas are good enough to make observations and test algorithms (See Chapter 3). A picture of the VSA can be seen in Figure 2.1.



Figure 2.1: The BYU Very Small Array (VSA).

Table 2.1: VSA antenna specifications. The 3 dB beamwidth, gain, and highest sidelobe level are from a simulation using a circular waveguide feed with a diameter of 1.3 wavelengths at 1612 MHz (see Chapter 4).

| | |
|--------------------------------|-------------|
| Diameter (D) | 120 inches |
| Focal Length (F) | 45.6 inches |
| F/D Ratio | 0.38 |
| 3 dB Full Beamwidth at 1.6 GHz | 5° |
| Gain | 29 dBi |
| Highest Sidelobe Level | -4 dBi |

2.2 RF Receiver

As mentioned in the previous section, a low-noise RF receiver was needed in order to make observations and test various algorithms. Brett Walkenhorst designed the original RF receiver [15] and modifications were later made by me in order to improve its performance (See Section 3.1). The final receiver includes commercially available parts as well as two custom filters. A system block diagram including a power budget can be seen in Figure 2.2.

The most important element of the receiver is the front-end low noise amplifier (LNA). Having a high quality LNA decreases the system noise temperature which makes it possible to detect faint radio sources. The first stage LNA was custom built by Richard Bradley at NRAO. In the system block diagram this is labelled as LNA1. This LNA has a noise temperature of 50 K and a gain of 18 dB. This amplifier is also broadband, with an operating frequency of 1.2-1.8 GHz with small variations in noise temperature and gain across this entire band. This LNA has made astronomy observations possible using the VSA platform.

In the system block diagram, LNA2, Amp, Mixer1, Mixer2 LPF1, and LPF2 are inexpensive components purchased from Mini-Circuits. BPF1 and BSF were designed using the design guide in HP ADS. More detail on BPF1 are given in Section 3.1. The bandstop filter (BSF) used is a microstrip stub low pass filter. The details of its design can be found in [15]. It was designed to reject the first stage images, and the second bandpass filter (BPF2) was used to reject the second stage images. The first intermediate frequency (IF) band is between 824-850 MHz and the final IF band is between 8-24 MHz. These components can be seen on a picture of one of the original RF receivers (Figure 2.3).

The final RF signals are input into Pentek digital receiver boards. These boards have an analog tuneable amplifier of up to 30 dB, as well as a 25 MHz low-pass anti-aliasing filter. After the signal passes through these components, the signal is sampled by the A/D converter and passed to the DSP boards for processing.

All of the RF receiver components were placed on microwave laminate circuit board using a coplanar design. A coplanar design was chosen for a few important

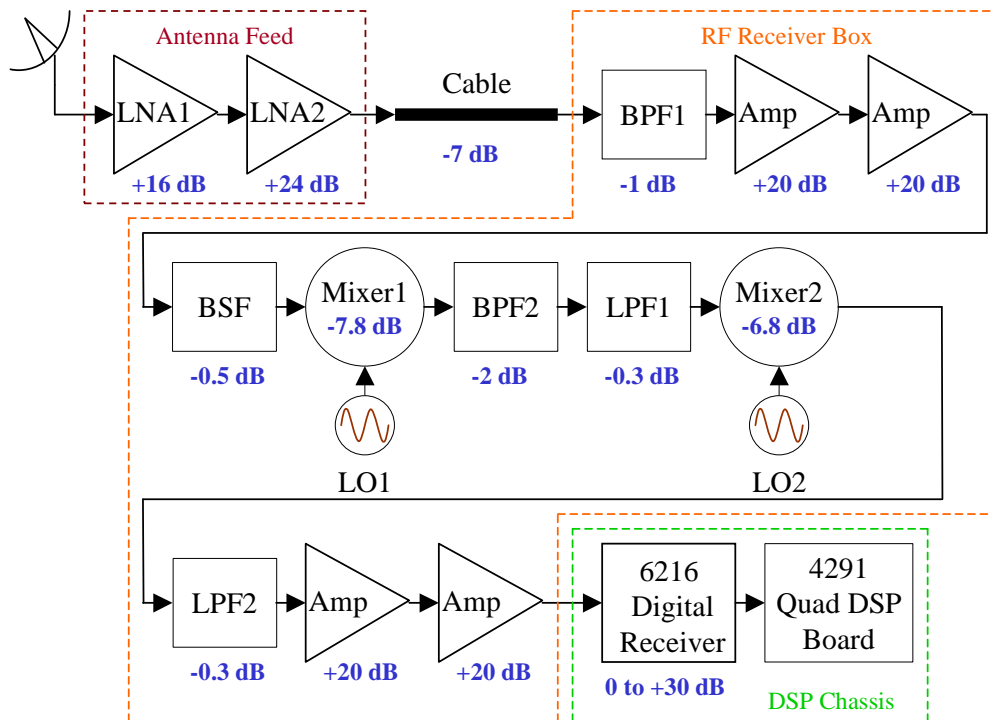


Figure 2.2: The system block diagram of the radio telescope VSA receiver, including the power budget. Several filters (BP=band pass, LP=low pass, and BS=band stop) are included in the design for signal image and out-of-band interference rejection. BPF2 is a surface acoustic wave (SAW) filter. The 6216 digital receiver provides 30 dB of tunable gain.

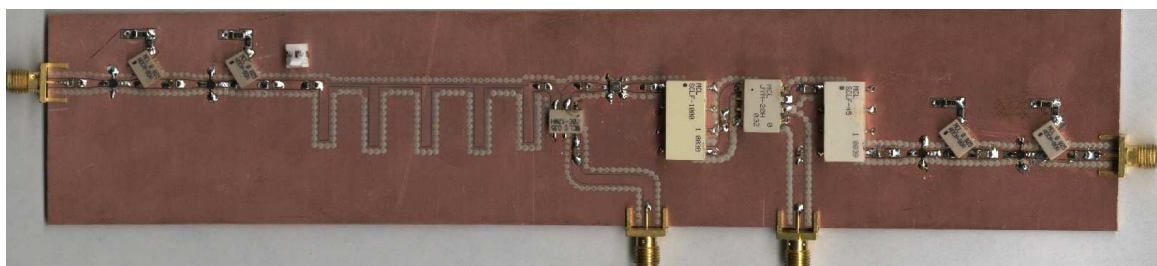


Figure 2.3: Picture of the original receiver design using coplanar technology.

reasons. It is inexpensive and can be quickly manufactured in our microwave laboratory. It also offers an easy solution for the grounding of transistors. In microstrip, a via through the dielectric is needed to connect ground pins from components to the bottom ground plate. This via creates an additional short transmission line which can cause mismatches and loss of power. Coplanar design has a ground plane next to the signal line, eliminating the need for vias to the chip pins.

The vias around the signal traces have another purpose. They help prevent electric fields from being launched into the substrate creating parallel plate modes. The vias also help eliminate crosstalk between the signal lines. Some problems were encountered with the vias and were corrected as explained in Section 3.1. Another advantage to a coplanar design is that the signal power is concentrated in the gaps between the signal traces and the ground plane. Thus the signal power will radiate less than a microstrip design, and creates less crosstalk with other nearby receiver boards. Figure 2.4 shows the electric fields in a microstrip and coplanar waveguide design. One can see that the fields in the coplanar design do not radiate as much as the fields in the microstrip design.

2.3 Sensitivity

The most important characteristic of any antenna to a radio astronomer is its sensitivity. Essentially, sensitivity tells a radio astronomer the smallest signal he can see without integration. It is defined as the antenna gain divided by the total system temperature,

$$S \text{ (Jy}^{-1}\text{)} = \frac{G(\text{K/Jy})}{T_{sys}(\text{K})} . \quad (2.1)$$

The system temperature (T_{sys}) is the sum of receiver, spillover, atmospheric, and cosmic background temperatures,

$$T_{sys} = T_{receiver} + T_{spill} + T_{atmosphere} + T_{cosmic} \quad (2.2)$$

where

$$T_{spill} = (1 - \eta_{spill})T_{ground} . \quad (2.3)$$

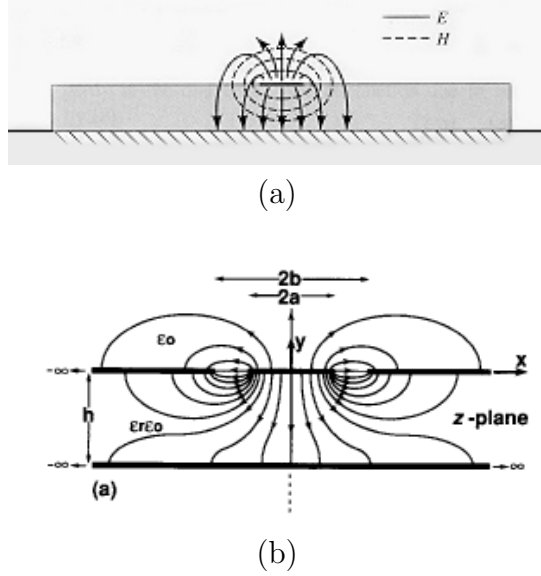


Figure 2.4: (a) Diagram of the transverse electric fields in a microstrip waveguide. (b) Diagram of the transverse electric fields in a coplanar waveguide (Figures used from [16, 17]).

Spillover efficiency is defined as the percentage of power of the array gain response that is collected by the reflector dish antenna,

$$\eta_{spill} = \frac{P_{dish}}{P_{tot}} \quad (2.4)$$

where P_{dish} is the power collected by the reflector dish and P_{tot} is the total radiated power by the array.

In most antenna applications system temperature is important, but not as important as it is in radio astronomy applications. This is because usually the power level of the signal of interest is very small, generally below the noise power. Sensitivity is most commonly displayed in units of inverse Jansky (Jy^{-1}). Another useful parameter to astronomers is the smallest detectable signal level, given as the inverse of sensitivity in units of Jy. Increasing the sensitivity of a radio astronomy receiver makes it possible to see smaller signal levels.

Gain is most commonly given as a dimensionless quantity. In order to convert from gain as a dimensionless quantity to gain in units of K/Jy, we first determine

effective aperture area,

$$A_e = \frac{G\lambda^2}{4\pi} \quad (2.5)$$

and then compute

$$G(\text{K/Jy}) = A_e \frac{10^{-26}}{k} \quad (2.6)$$

where $1 \text{ Jy} = 10^{-26} \text{ W/m}^2/\text{Hz}$ and k is Boltzman's constant.

2.4 Multiple Feed Arrays in Radio Astronomy

Traditionally, radio astronomy reflector dishes use a single waveguide or horn feed. The feed is designed to have a high spillover efficiency while still producing high gain [18]. This enables radio astronomers to observe smaller signals. The single waveguide feed is an effective method for radio astronomy observations, and a great deal of research has gone into the design of waveguide feeds for use in radio astronomy.

Radio astronomers are constantly trying to improve the efficiency of astronomical observations. One method is to increase the number of receivers or feeds in a single radio telescope dish reflector. The theory for this concept has been available for over 30 years [19]. Multiple feed arrays offer several advantages over traditional feed types. Array feeds can be used to compensate for reflector aberrations, improve the efficiency of off-axis beams, achieve shaped antenna patterns, and electronically synthesize multiple scanned beams for rapid sky coverage [20, 21, 22]. Multiple feed arrays have also been used in communication receivers and satellites. In some communication satellites each feed in the array is designed to operate at a different frequency [23]. There has been a great deal of research in array feed design for communication satellites [24, 25, 26, 27].

A great deal of research has gone into studying multiple feed array systems, and a few implementations have already been made. In 1995 a special workshop was organized to study multiple feed systems [28]. Most commonly, array feeds in radio astronomical applications have employed electrically large, waveguide-type elements with minimal or no signal combining between elements. The multibeam receiver on the Parkes telescope in Australia is an example, using many waveguide feeds placed



Figure 2.5: Picture of the Parkes 13-element waveguide array feed [30].

in the focal plane of the dish [29]. Figure 2.5 shows a picture of the Parkes array. By using such an array, astronomers are able to do rapid sky surveys, thus reducing observation times.

Two advantages waveguide array feeds have over other feeds is that no array processing is required, and each element is optimized for high sensitivity. This makes the overall system less complicated and easier to implement. There are some problems encountered when using large waveguide feeds in an array. Because of their size, the spacing between elements is large. This causes an undersampling of the far field power [21]. Waveguide feeds are only well matched to the focal plane fields near the optical axis of the telescope.

There has been a great deal of research and work involving active array feeds outside of radio astronomy. Some commercial communications satellite systems use phased array feeds in conjunction with a reflector dish antenna [31]. Phased array feeds have been used in radar applications for wide-angle scanning and to improve the efficiency of off-axis beams of large-aperture reflectors [20]. They are also used to correct reflector surface distortions [20]. A receiver system using a phased array feed is complex and requires some type of array processing. A great deal of research has gone into improving array processing speeds and capabilities on a phased array feed [32]. Some have attempted to simplify the array processor by only using phase shifters [33]. Others have used phased array feeds to correct for pattern distortions caused by malfunctions in other parts of the receiver system [34]. Phased array feeds are unique in that beamscanning can be done electronically [35]. This provides the capability of forming multiple beams simultaneously [36].

There has been some research on phased array feeds within the field of radio astronomy. Many of the papers published in [28] dealt with phased array feeds. NRAO has also put great effort into studying phased array feeds [21, 37, 38, 39, 40]. NRAO has proven that a full-sampling focal plane array can be designed using electrically small elements [40]. NRAO built a prototype array receiver based on this research. The array consisted of 19 sinuous antenna elements and can be seen in Figure 2.6. This array was used to form multiple beams.

None of these phased array feed implementations have been used for RFI mitigation. Chapter 5 demonstrates that RFI mitigation is possible using a phased array feed.

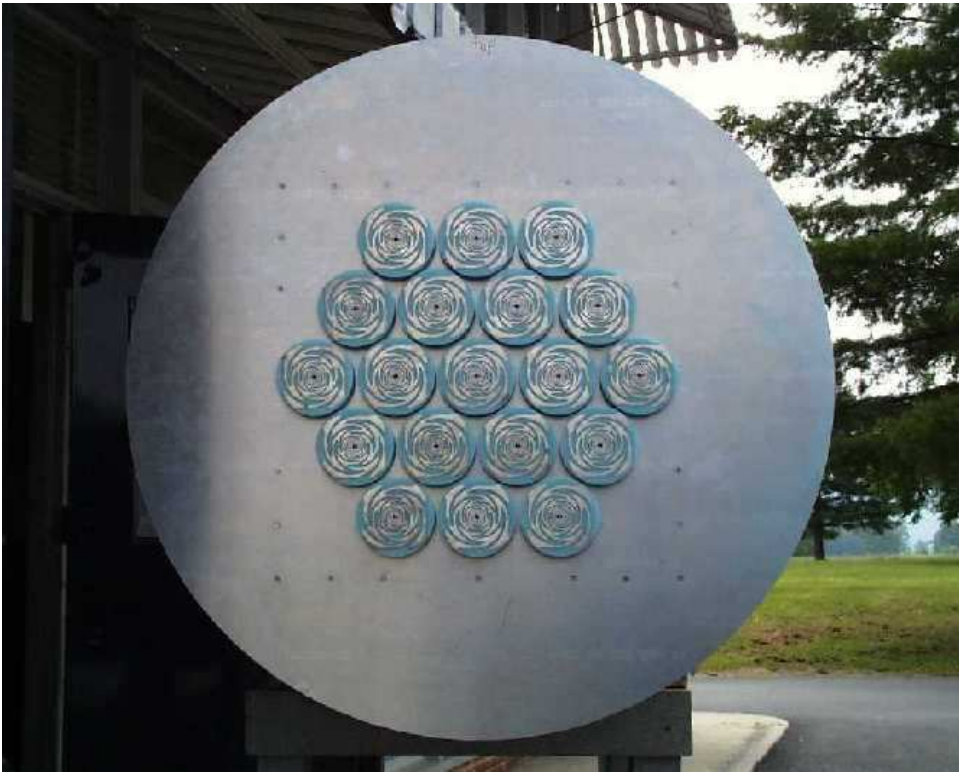


Figure 2.6: Picture of the 19-element array feed implemented at NRAO. [41].

Chapter 3

Receiver Improvements and VSA Observations

A great deal of work went into improving the RF receiver discussed in Section 2.2. When the VSA was tested initially no celestial sources could be detected. The largest problem was the high level of noise leaking through the receiver system. Several receiver improvements made it possible to make observations using the VSA.

3.1 RF Receiver Improvements

There were a few problems that were encountered with the original receiver [15]. We discovered two corrupted bands in the final IF. These bands occurred with LO2 stationary at 816 MHz and LO1 in one of two bands, 2424-2440 MHz and 2456-2472 MHz. Walkenhorst attributes this to LO1 leaking through and mixing with the 3rd harmonic of LO, even though LO1 should have been attenuated by LPF2.

It was discovered that harmonic mixing was the cause of the corrupted bands which were leaking through the receiver board. The vias in the board were not working properly and should have attenuated any stray signals. To resolve the problem, many holes were drilled around the signal lines and the two ground planes were connected with many short copper wires. This significantly reduced the signal leakage, but did not completely eliminate it. However, by adjusting the frequencies of the LOs any frequency band could be observed.

The first attempts at observing an astronomical source yielded a very high noise level due to noise outside of the frequency band of interest entering the receiver. A bandpass filter (BPF1) was designed to eliminate the problem. This filter was designed using the Design Guide in HP ADS. Several prototypes were built and

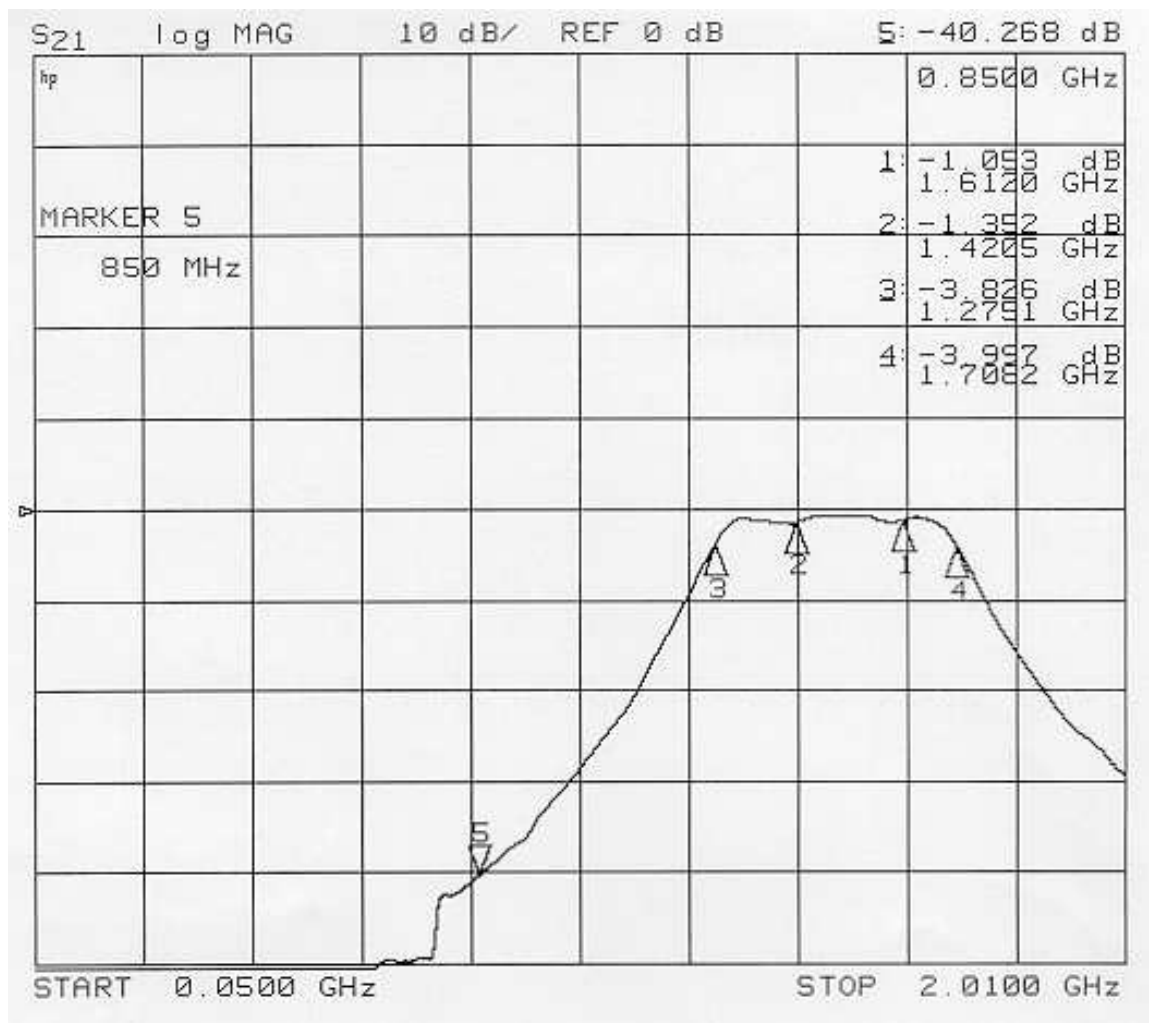


Figure 3.1: Frequency response of the first bandpass filter.

the design was adjusted to produce the best results. A filter was produced with a passband of 1.3-1.7 GHz (See Figure 3.1). It was difficult to produce a good filter with a passband of 1.2-1.8 GHz, so the overall bandwidth was decreased. This did not cause a large problem because most of the VSA observations will be within this band. Integrating the filter into the RF receiver decreased the noise floor of the final output and the signal-to-noise ratio (SNR) of the GLONASS signal increased significantly.

Another important improvement was the addition of large 1 W power resistors and bypass capacitors to all of the voltage sources on the receiver. Two amplifiers on

different prototype boards blew out, most likely because the resistors were dissipating too much power. The addition of the resistors eliminated this problem. It is possible that some of the signal leakage mentioned earlier was occurring because the signal was coupling with the power line traces on the receiver boards. In an application note by Mini-Circuits [42], the author advises the use of a bypass capacitor from the input voltage to ground to prevent any coupling to other parts of the board. The use of RF chokes should prevent most RF signals from leaking back into the power supply, but it is possible for small levels to leak through the choke. Using bypass capacitors helps ensure these stray signals cannot enter the power supply and corrupt other components on the receiver board. High quality broadband DC blocking capacitors were used for the bypass capacitors.

Once all four receivers were finished, they were placed inside a chassis for ease of use (See Figure 3.2(b)). It was discovered that there was cross-talk between the different receiver boards within the chassis. To eliminate this problem, RF-absorbent material was placed in between the receiver boards, as well as all around the inside of the chassis. This eliminated almost all of the cross-talk between the receivers. A picture of the four channel receiver can be seen in Figure 3.2(b). Figures 3.2(a), (c), and (d) show pictures of other components of the VSA test platform.

Improvements were made to the first and second stage LNAs to improve the system noise temperature. A Mini-Circuits standard LNA was tested at the Central Development Lab at NRAO and found to have a very low noise figure, approximately 110 K. It had a lower noise figure and higher gain than the previous second stage LNA, made by Agilent. The Agilent LNAs were all replaced.

Another inexpensive LNA with a noise figure of 28 K was used. This LNA was custom made with a center frequency of 1612 MHz. However, it only has a bandwidth of approximately 50 MHz. This LNA is ideal for observing OH Masers and GLONASS satellites. Combining this LNA with the Mini-Circuits LNA reduces the overall system temperature from 52 K to 31 K. See Table 3.1 for a list of the final RF receiver specifications.

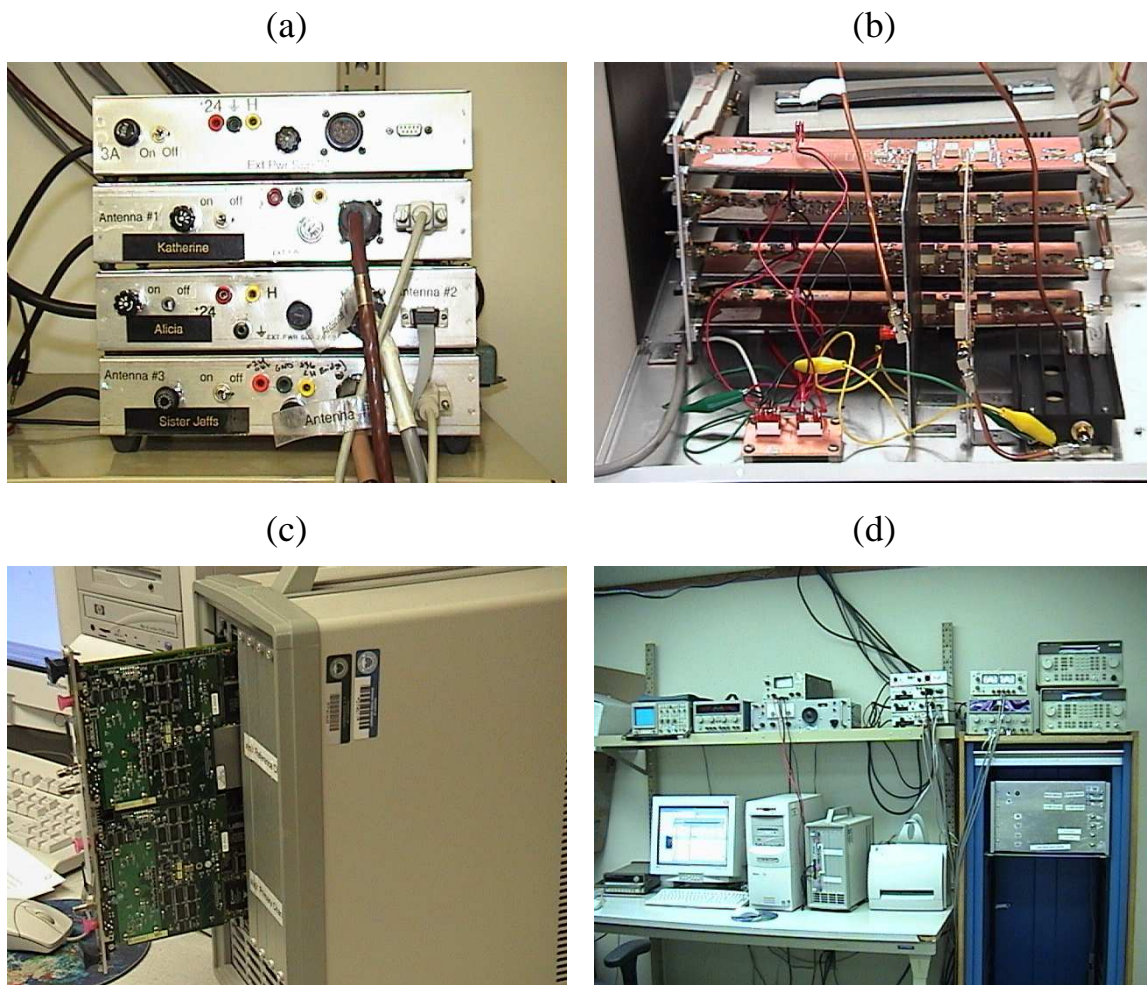


Figure 3.2: (a) Antenna positioning hardware used to steer the VSA antennas. (b) Four channel RF receiver system. (c) Real-time DSP platform. (d) BYU VSA control/receiver station.

Table 3.1: RF receiver specifications.

| | |
|--|---|
| Operational Frequency | 1.3–1.7 GHz |
| Final IF Center Frequency | 8–24 MHz |
| IF Bandwidth | 16 MHz |
| System Gain | 94-124 dB |
| System Noise Temperature (Calculated) | 52 K (wide-band LNA) 31 K (1612 MHz narrow-band LNA) |

3.2 VSA Observations

Once the receiver was working properly, several observations were made. The VSA was used to test DSP code under development. We were able to look at the spectrum of several different satellite signals as well as different astronomical sources. One of the first successful observations was a GLONASS satellite.

Figure 3.3 is one example of the several observations that were made. It demonstrates the fine structure of the frequency modulation, especially around its center frequency of 1606 MHz. This type of modulation can be seen in other GLONASS satellite observations [6].

Two other observations can be seen in Figure 3.4. This plot shows the frequency spectrum of two well known radio sources. This is the sampled data taken at the DSP. Figure 3.4(c) shows the receiver output with RF absorber placed in the feed of the dish antenna. We did this in order to measure a baseline, and demonstrate that the observed spectrum was coming from the sources and not generated internally within the receiver. This was also a good check on our overall system. Since the RF absorber is essentially a black body radiator at ambient temperature, the total received power should be higher than when looking at faint astronomical sources, which it is. The output power was checked for a black body radiator. The output power is found from $P = kTB$ where k is Boltzman's constant, 1.38×10^{-23} J/K, T is the temperature, and B is the bandwidth. For $T=300$ K, $P = -173.8$ dBm/Hz. The receiver has approximately 95 dB of gain which means the total power at the DSP should be -78.8 dBm/Hz. The measured results agree with this number as can be seen in Figure 3.4(c). The slant in the figure is due to the receiver gain variation. By subtracting the baseline the exact frequency spectrum of the two sources can be obtained as shown in Figure 3.5.

Another important test involved the use of two separate reflector antennas from the VSA. All of the previous observations had used only a single dish and receiver. This test used a least-mean-square (LMS) algorithm to subtract out an interferer in real time. Figure 3.6 shows the results of one of these tests. The details of the LMS algorithm implementation on the DSP can be found in [12]. The LMS algorithm uses

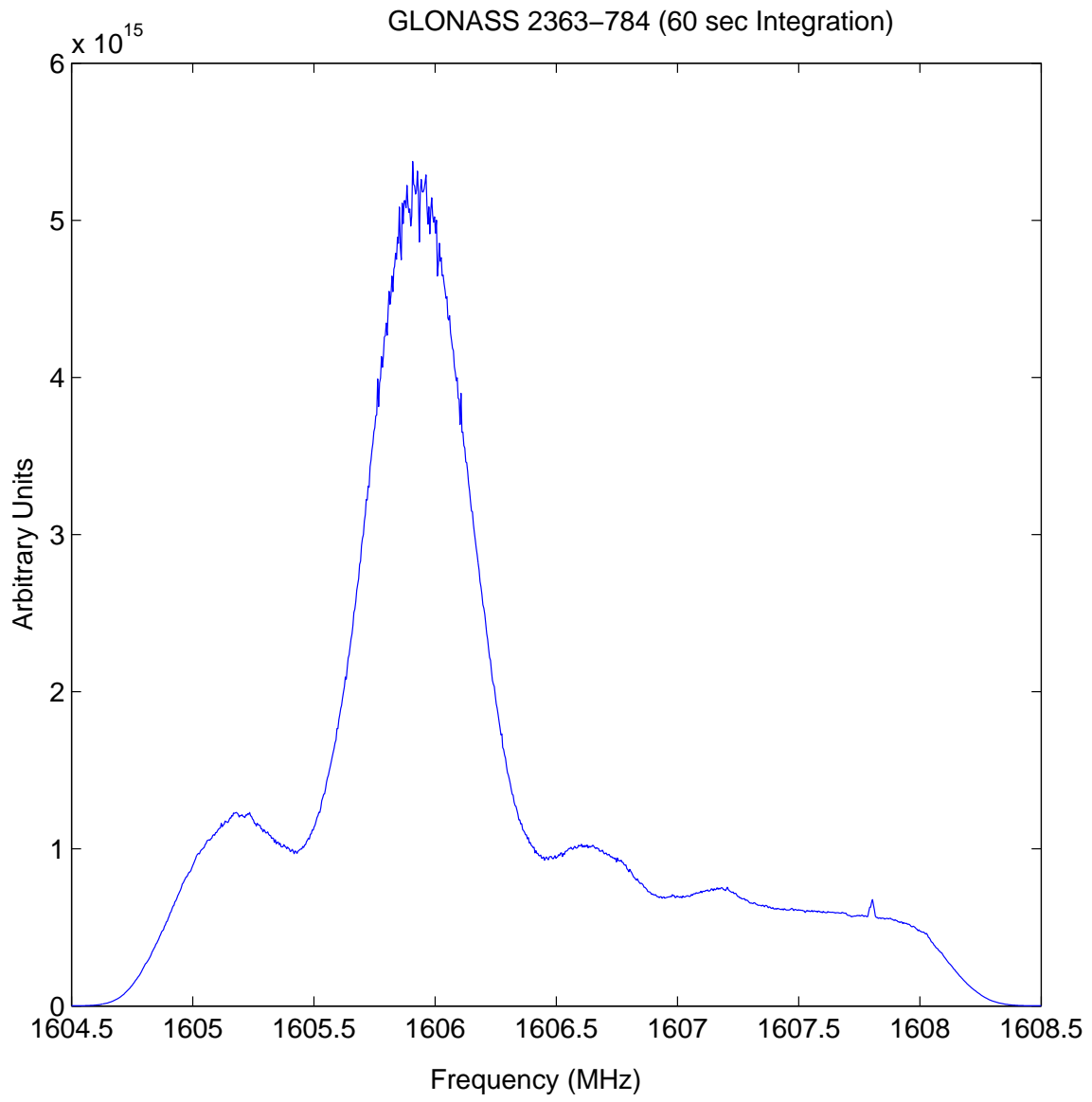


Figure 3.3: Frequency spectrum of a GLONASS satellite.

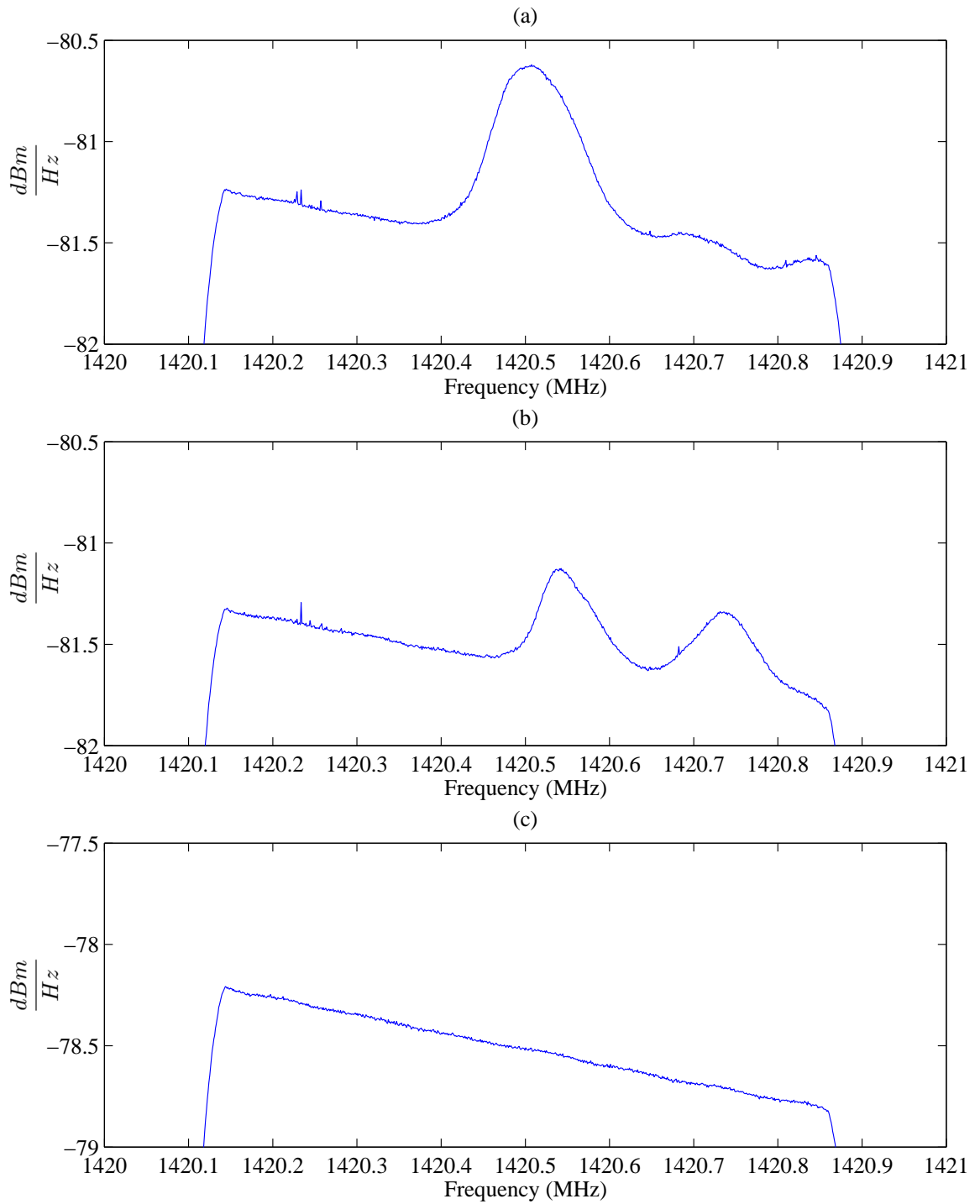


Figure 3.4: VSA observations of the (a) Frequency spectrum of Cygnus. (b) Frequency spectrum of Casseioipia. (c) Frequency spectrum of black body radiation from RF absorber.

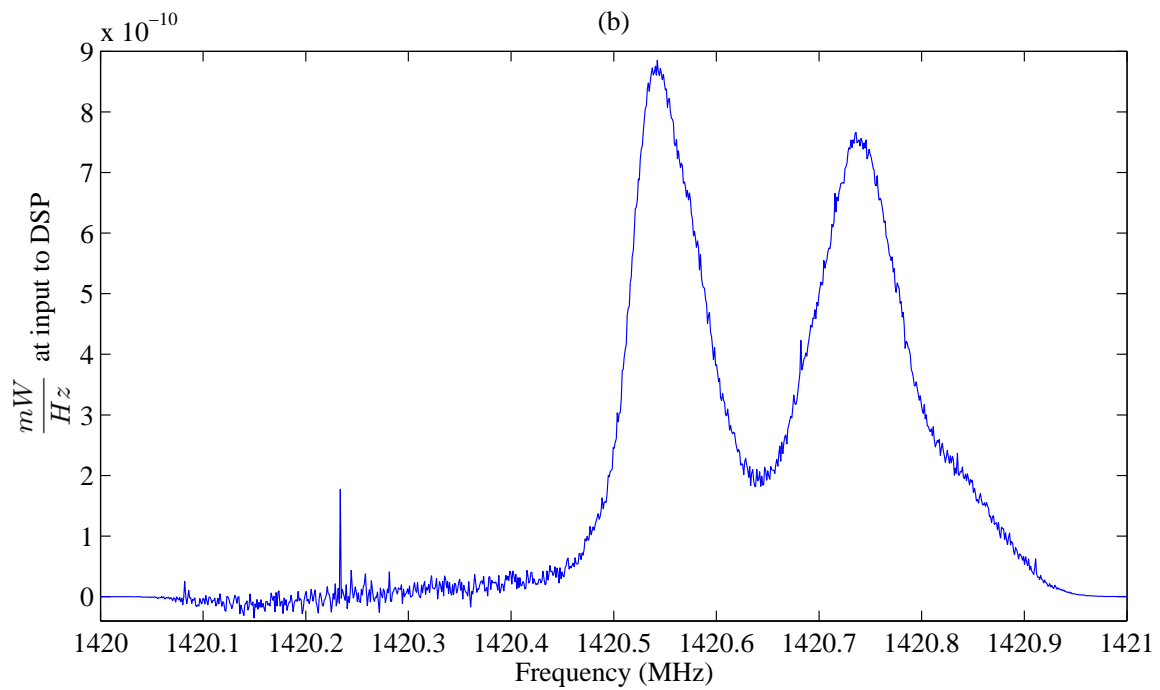
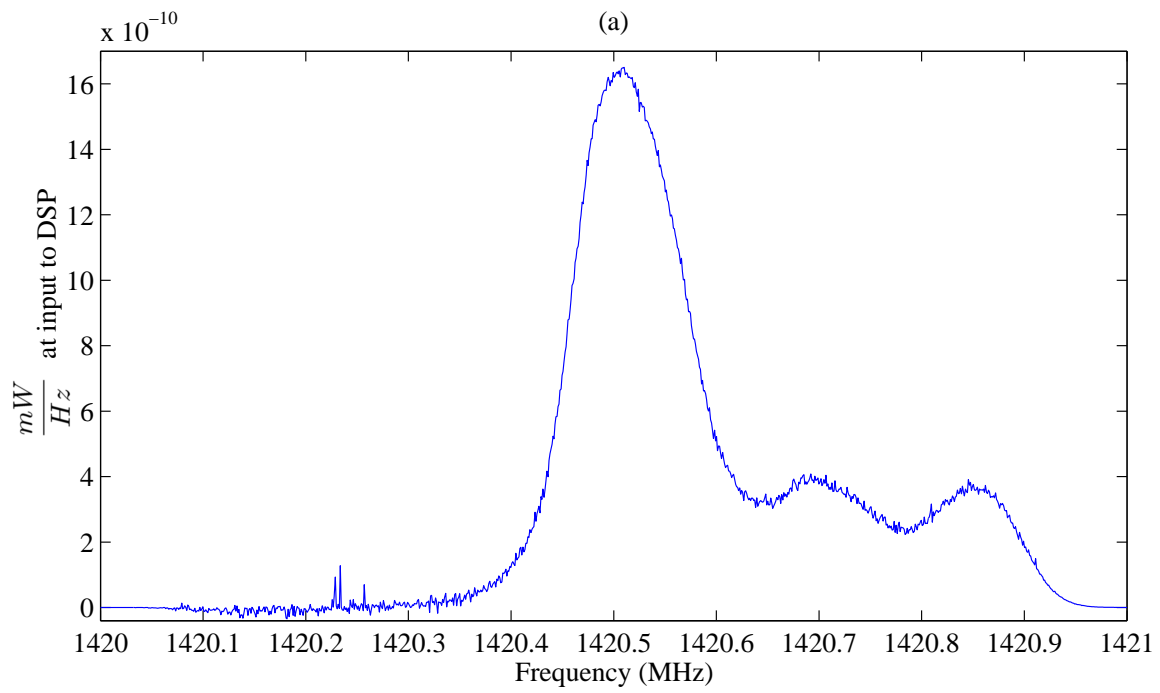


Figure 3.5: VSA observations of the (a) Frequency spectrum of Cygnus. (b) Frequency spectrum of Casseioia.

both a primary and a reference channel. The primary antenna is pointed at the source, and receives some of the interference power through its sidelobes. The reference antenna is pointed at the interference and thus receives a high interference-to-noise ratio. The LMS filter essentially works by subtracting the reference channel from the primary channel, leaving only the signal of interest. Cygnus was the observation source, and the interference was produced by an FM sweep from a signal generator. We placed a $1/2$ wavelength dipole antenna on top of an observation tower and pointed it towards the reference antenna. The algorithm worked very well on this test. Figure 3.6(a) shows that the interference was completely removed from the primary channel, leaving only the signal of interest.

This test verified many parts of the VSA test platform. It showed that two channels functioned properly simultaneously. The test showed there was very little cross-talk between the receivers. If there had been, some of the signal would have been subtracted as well. To our knowledge, this was the first time that an LMS adaptive algorithm had been used in real-time for a radio astronomy application. The DSP code and DSP platform were later used to effectively cancel satellite interference at the Green Bank Telescope. The details of this experiment can be found in [12] and [13].

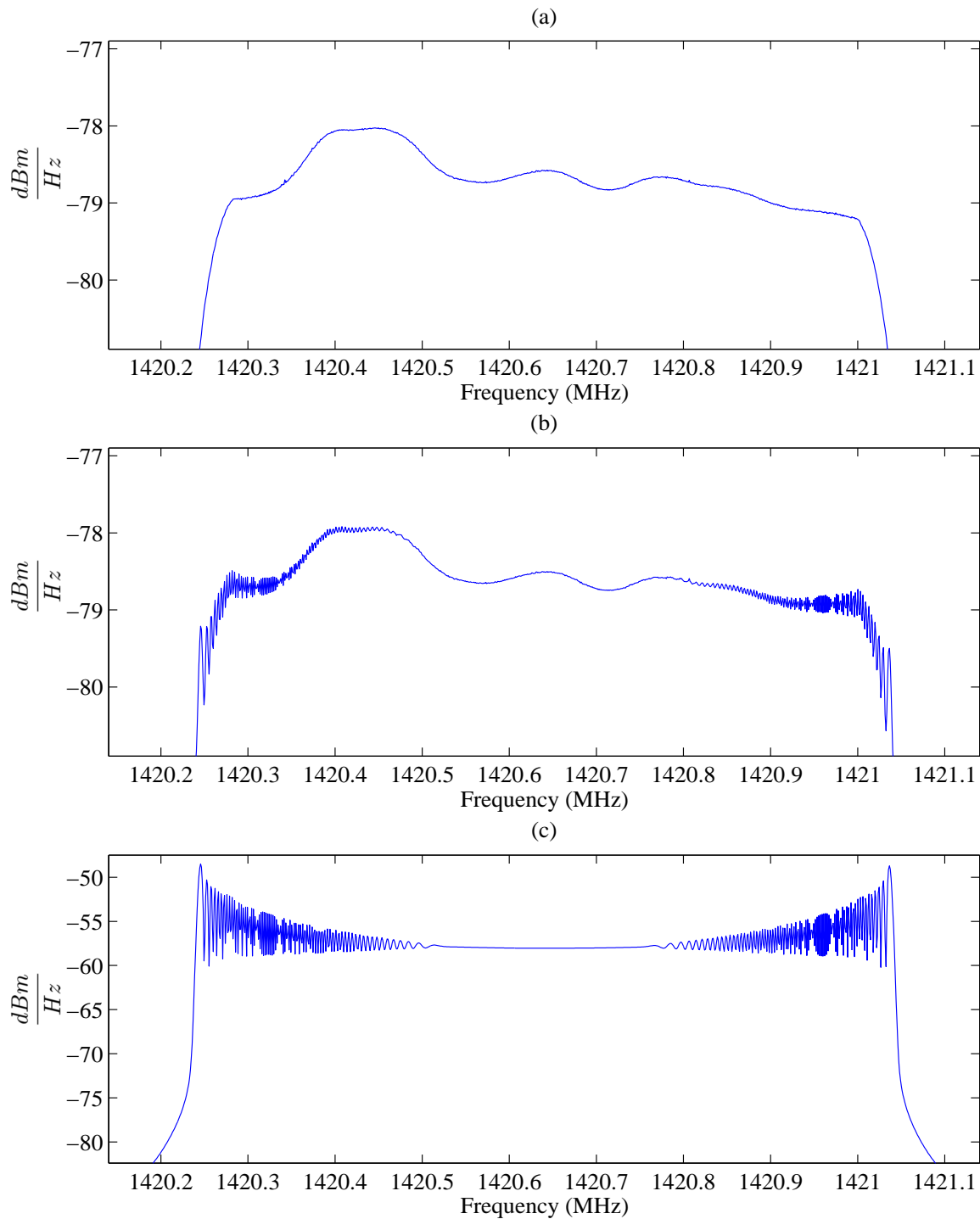


Figure 3.6: Results of one LMS test on the VSA. (a) Power Spectral Density (PSD) estimate of the filtered output after subtracting the interference. Note that the interference is undetectable in the spectral baseline. (b) PSD estimate of the primary channel. This includes the power from both the signal of interest and the interferer. The spectral hydrogen line is that of Cygnus corrupted by an FM sweep interferer. (c) PSD estimate of the reference channel. Only the power from the interferer is received.

Chapter 4

Sensitivity Optimization with Multiple Feed Array

4.1 Simulation Parameters

For all of the simulations provided in this thesis, the following parameters are used. Sensitivity is defined as the antenna gain divided by the total system temperature as seen in Eq. 2.1. In the system temperature,

$$T_{receiver} = 15 \text{ K} \quad (4.1)$$

$$T_{atmosphere} = 0 \quad (4.2)$$

$$T_{cosmic} = 0 \quad (4.3)$$

$$T_{spill} = (1 - \eta_{spill})T_{ground} \quad (4.4)$$

where

$$T_{ground} = 300 \text{ K} . \quad (4.5)$$

The noise temperatures due to the atmospheric and cosmic background radiation can be neglected because their contribution is small compared to the receiver and spillover temperatures.

Sensitivity is sometimes stated with the amount of integration time required to achieve it. When integration is performed on the beamformer output, the variance of the noise floor decreases, producing a higher sensitivity. For all of the simulations and results that follow, sensitivity is given with an integration time of zero, thus assuming an instantaneous measurement.

4.2 Phased Array Feed Gain

As mentioned in Section 2.4, NRAO has worked on developing a phased array feed to be used for radio astronomy observations. It was the desire of the BYU Radio Astronomy Research Group to help in this development and use such an array in interference mitigation. In order to design and simulate an array we needed a software package that would produce accurate gain and phase patterns. We used a student version of TICRA's GRASP8 antenna simulation package to calculate the gain patterns. GRASP8 uses physical optics (PO) and the physical theory of diffraction (PTD). For a detailed explanation of single feed gain pattern computations using GRASP8 see Appendix A. The process of finding the directivity of a phased array feed on a reflector antenna is slightly more complicated, since the total power radiated needs to be calculated. The first step is to find the radiated electric field E_{rad} for each element in the array. This is accomplished by finding the scattered electric field E_{scat} from the reflector dish due to each element. E_{rad} is then found by adding E_{scat} with the incident electric field E_{inc} from each element,

$$E_{rad,n} = E_{scat,n} + E_{inc,n} . \quad (4.6)$$

The total electric field E_{tot} is found by multiplying each field by its corresponding weight and adding up the fields,

$$E_{tot} = \sum_1^N w_n E_{rad,n} . \quad (4.7)$$

The total power radiated is found by integrating the total electric field over a sphere,

$$P_{rad} = \int_0^{2\pi} \int_0^\pi \frac{|E_{tot}|^2}{2\eta} r^2 \sin\theta d\theta d\phi . \quad (4.8)$$

The gain of the phased array plus reflector can then be found from

$$G(\theta, \phi) = \frac{|E_{tot}(\theta, \phi)|^2 / 2\eta}{P_{rad} / 4\pi r^2} . \quad (4.9)$$

The integrals are performed numerically using 180 sample points in the θ direction and 360 sample points in the ϕ direction.

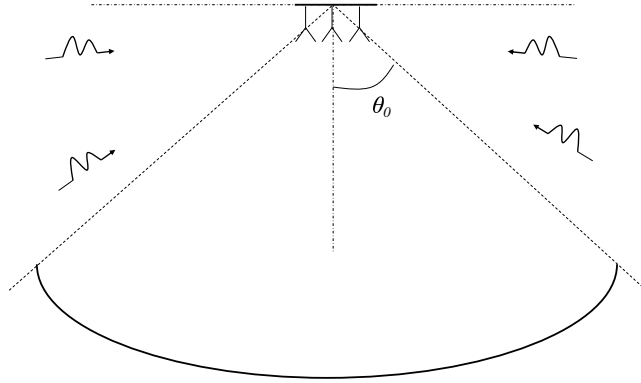


Figure 4.1: Spillover noise entering the array feed from the background.

4.3 Spillover Efficiency

Spillover efficiency is defined as the percentage of power of the array gain response that is collected by the reflector dish antenna,

$$\eta_{spill} = \frac{P_{dish}}{P_{tot}} \quad (4.10)$$

where

$$P_{dish} = \int_0^{2\pi} \int_0^{\theta_0} \frac{|E_{tot,feed}|^2}{2\eta} r^2 \sin \theta d\theta d\phi \quad (4.11)$$

$$P_{tot} = \int_0^{2\pi} \int_0^{\pi/2} \frac{|E_{tot,feed}|^2}{2\eta} r^2 \sin \theta d\theta d\phi . \quad (4.12)$$

$|E_{tot,feed}|^2$ is the gain response of the array feed without the reflector as defined below and θ_0 is the angle to the edge of the reflector dish as seen in Figure 4.1. This figure demonstrates that the higher the spillover efficiency the lower the noise entering the array from the surrounding area.

To find the gain response of the array feed without the reflector, the individual element responses must first be found. In general, the radiated electric far field due to a single current source is given by [43]

$$\bar{E}(\bar{r}) = -j\omega\mu \frac{e^{-jk r}}{4\pi r} (\hat{\theta} f_\theta + \hat{\phi} f_\phi) \quad (4.13)$$

where

$$\bar{f}(\theta, \phi) = \int d\bar{r}' \bar{J}(\bar{r}') e^{j\bar{k} \cdot \bar{r}'} . \quad (4.14)$$

For a Hertzian dipole oriented in the \hat{x} direction,

$$\bar{f}(\theta, \phi) = \hat{x}Il = (\hat{r} \sin \theta \cos \phi + \hat{\theta} \cos \theta \cos \phi - \hat{\phi} \sin \phi)Il \quad (4.15)$$

where Il is the current dipole moment. From Eq. 4.13 E_θ and E_ϕ can be found,

$$E_\theta = -j\omega\mu \frac{Il e^{-jkr}}{4\pi r} \cos \theta \cos \phi \quad (4.16)$$

$$E_\phi = j\omega\mu \frac{Il e^{-jkr}}{4\pi r} \sin \phi . \quad (4.17)$$

For an array of Hertzian dipoles,

$$E_{\theta,tot} = E_\theta F \quad (4.18)$$

$$E_{\phi,tot} = E_\phi F \quad (4.19)$$

where F is the array factor. F is found to be

$$F = \sum_{n=1}^N w_n e^{jk(x'_n \sin \theta \cos \phi + y'_n \sin \theta \sin \phi + z'_n \cos \theta)} \quad (4.20)$$

since

$$\bar{k} \cdot \bar{r}' = k(x' \sin \theta \cos \phi + y' \sin \theta \sin \phi + z' \cos \theta) \quad (4.21)$$

and w_n are the complex weights on the array elements. x'_n , y'_n , and z'_n are the coordinates of the n^{th} array element. The gain response of the array feed without the reflector is then found from

$$|E_{tot,feed}|^2 = |E_{\theta,tot}|^2 + |E_{\phi,tot}|^2 . \quad (4.22)$$

4.4 Antenna Parameters

The simplest candidate for an antenna element in a phased array feed is a dipole. NRAO is currently running simulations on two types of dipoles, folded and sleeved. The GRASP8 Student Edition software only allows the use of Hertzian dipoles. For this reason all of the simulations that follow use Hertzian dipoles as the feed array elements. The radiation pattern of a Hertzian dipole is very similar to that of other small dipoles, and therefore the qualitative results should apply to other types of dipoles.

Table 4.1: Simulated antenna specifications. The 3 dB beamwidth, gain, and highest sidelobe level are from a simulation using a circular waveguide feed of 1.3 wavelengths at 1612 MHz. The surface distortion is the RMS small scale surface deviation.

| | |
|--------------------------------|-----------------------------------|
| Diameter (D) | 25 m |
| Focal Length (F) | 9 m |
| F/D Ratio | 0.36 |
| Surface Distortion | .025 mm |
| 3 dB Full Beamwidth at 1.6 GHz | .5° |
| Gain | 49.8 dBi |
| Sensitivity | $7 \times 10^{-3} \text{Jy}^{-1}$ |
| Highest Sidelobe Level | 0 dBi |
| Average Sidelobe Level | -20 dBi |

The reflector dish used in the simulations is similar to one of the reflector dishes used at the Very Large Array (VLA) in New Mexico. It has the same diameter (D) and F/D ratio. The simulated dish is a parabolic dish, while the VLA type dishes are shaped reflectors. The VLA dishes are shaped to produce higher gain at the focal point. The simulated dish also has the same RMS small scale surface distortion as the VLA dishes. A summary of the simulated dish parameters can be seen in Table 4.1.

A hexagonal grid was chosen for the array because it produces the highest two-dimensional density of elements [44]. A spacing of 0.6 wavelengths was chosen for the array. This spacing fulfils the requirement to fully sample the focal plane fields [45]. It is also large enough that mutual coupling is not an overwhelming problem. Future research will analyze different spacings as well as the effects of mutual coupling on sensitivity and interference mitigation. Figures 4.2 and 4.3 show the reflector and array feed. A ground plane was not used for ease of simulation, but will be included in future work. It will be especially important in mutual coupling research. The student version of GRASP8 does not allow the simulation of support struts, which will have some effect on the beam pattern of the array, most notably in the sidelobes.

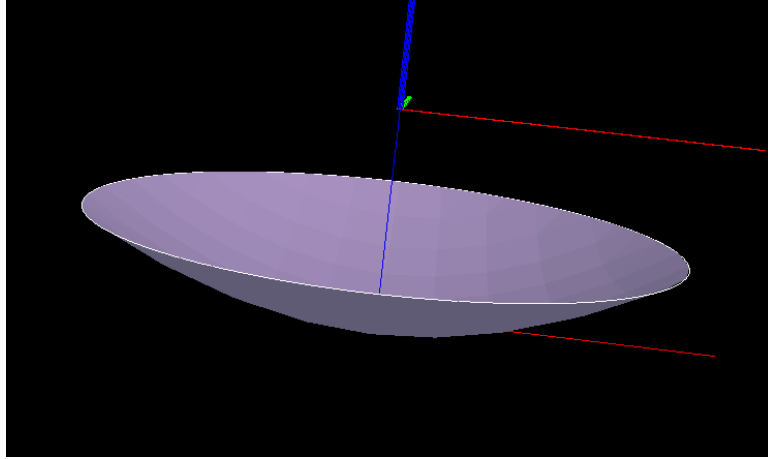


Figure 4.2: Picture of the reflector antenna. Colored lines correspond to the coordinate axis of the dish and each element in the array.

Future research should also include the effects of these struts. The beam pattern of the simulated antenna has an average sidelobe value of -20 dBi. By simulating the supports, the sidelobe level would most likely increase to around 0 dBi, a more realistic value for the VLA dishes.

4.5 Waveguide Standard

It was desired to have a baseline sensitivity value to which we could compare the array results. Simulations were performed using a circular waveguide feed of different sizes. We found the diameter that produced the highest sensitivity and used this feed as a comparison to the array feed results. A plot of sensitivity versus diameter of the feed can be seen in Figure 4.4. Figures 4.5 and 4.6 show the gain and spillover efficiency of these feeds. These plots illustrate the trade-off between gain and spillover efficiency in order to produce the highest sensitivity possible. The feed with the highest sensitivity has a diameter of 1.3λ .

Another important consideration was how to sample the beam pattern appropriately. If the beam pattern was not fully sampled, the integration of the total power radiated would not be accurate. It would also be difficult to simulate a moving

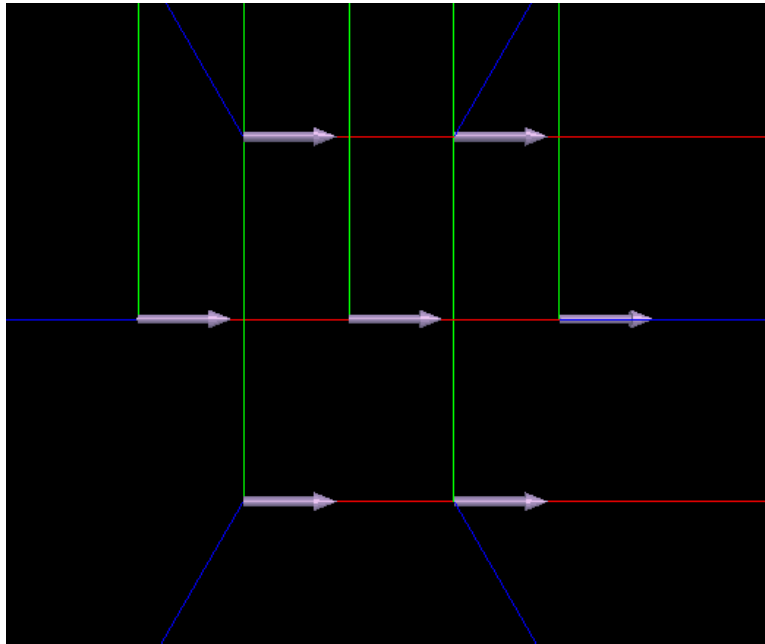


Figure 4.3: Hexagonal array feed.

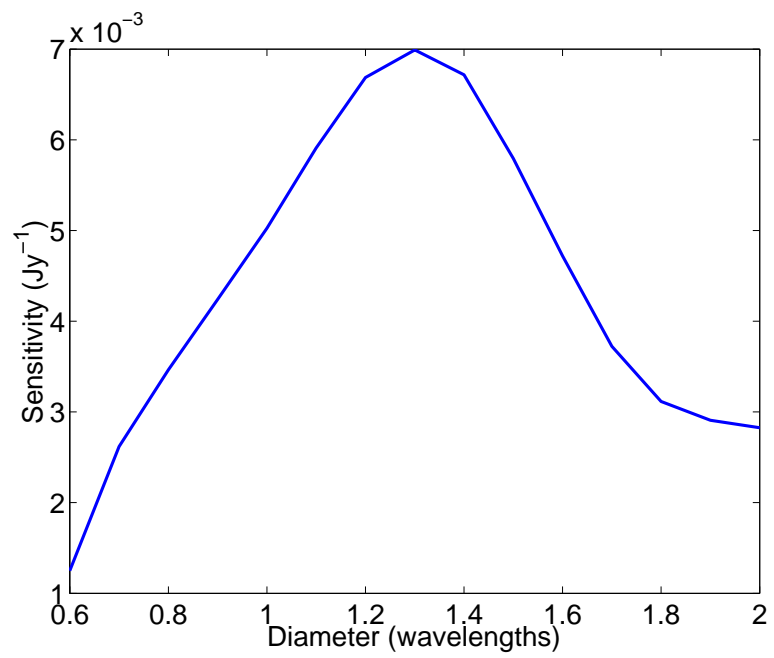


Figure 4.4: Sensitivity as a function of diameter of a circular waveguide feed.

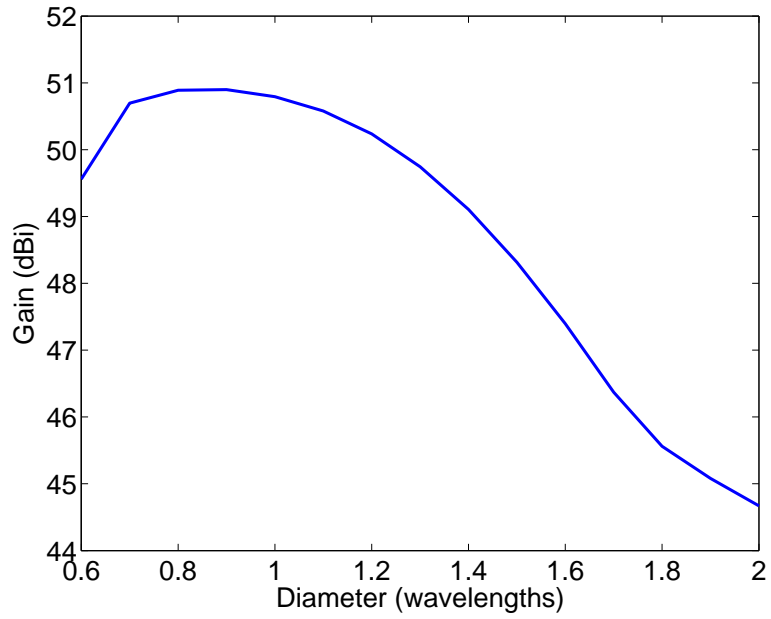


Figure 4.5: Gain as a function of diameter of a circular waveguide feed.

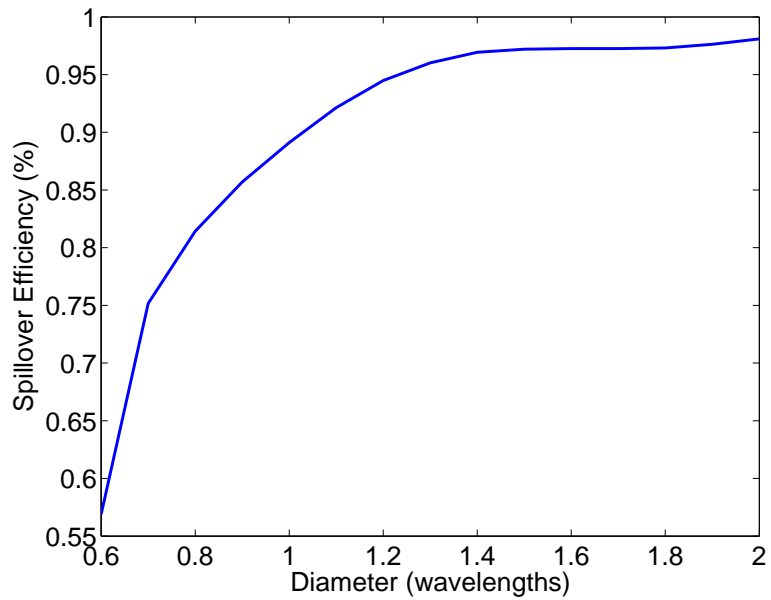


Figure 4.6: Spillover efficiency as a function of diameter of a circular waveguide feed.

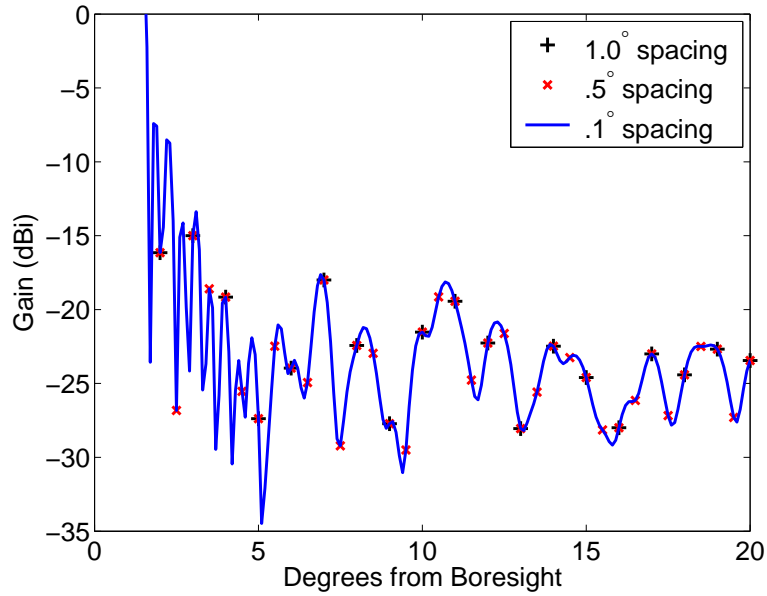


Figure 4.7: The beam pattern of a reflector dish with a waveguide feed sampled at 1° , $.5^\circ$, and $.1^\circ$.

interferer. Before simulating a large dish such as the VLA antennas, we studied a smaller dish, similar to the dishes used in the VSA at BYU. With the smaller dish it was only required to sample the pattern every 1° in both θ and ϕ directions. This sampling was not sufficient for the larger dish. Figure 4.7 shows part of the beam pattern with 1° , $.5^\circ$, and $.1^\circ$ sampling for a waveguide feed with a diameter of 1.3λ . From the figure, one can see that $.1^\circ$ sampling is enough to fully sample the beam pattern.

4.6 Beamforming

In general, a beamformer is a method of combining different spatial samples of a signal. The spatial samples are provided by different antenna elements, in this case different array feed elements. The beamformer is used to produce an array response with a high gain in the direction of the signal of interest while attenuating noise and interference arriving from all other directions. Beamforming can be done on

both broadband and narrowband signals, but the following discussion applies only to narrowband signals.

As can be seen from Figure 4.8 a beamformer combines the spatial samples in the following manner:

$$\mathbf{y} = \mathbf{w}^H \mathbf{x} \quad (4.23)$$

where $\mathbf{w} = \begin{bmatrix} w_1 & w_2 & \cdots & w_N \end{bmatrix}^T$ is a vector containing the complex array weights and $\mathbf{x}[n] = \begin{bmatrix} x_1[n] & x_2[n] & \cdots & x_N[n] \end{bmatrix}^T$ is a vector containing the sampled signals of the array elements. There are many different methods for selecting the element weights, each with a different criterion. These methods are used to produce a large array response in the direction of interest and a small response in the direction of interferers and noise.

For a given frequency, the beamformer response is given by

$$r(\theta, \phi) = \mathbf{w}^H \mathbf{d}(\theta, \phi) \quad (4.24)$$

where

$$\mathbf{d}(\theta, \phi) = \begin{bmatrix} A_1 e^{j\Phi_1}(\theta, \phi) & A_2 e^{j\Phi_2}(\theta, \phi) & \cdots & A_N e^{j\Phi_N}(\theta, \phi) \end{bmatrix}^T. \quad (4.25)$$

A_i and Φ_i are the amplitude and phase responses of the individual array elements in conjunction with the reflector dish antenna. The final beampattern of the array feed is given by

$$g(\theta, \phi) = |r(\theta, \phi)|^2. \quad (4.26)$$

$g(\theta, \phi)$ has the same response of $G(\theta, \phi)$ in Eq. 4.9 except for an amplitude shift. The element weights can be normalized such that $g(\theta, \phi) = G(\theta, \phi)$.

4.7 Sensitivity Optimization

Our primary goal in the design of an array feed was to optimize the array for RFI cancellation while also achieving high sensitivity and beam steering capability. The phased array feed should produce a higher sensitivity as compared to a single standard waveguide feed. Other design goals include gain stability and low beam shape distortion for steered beams.

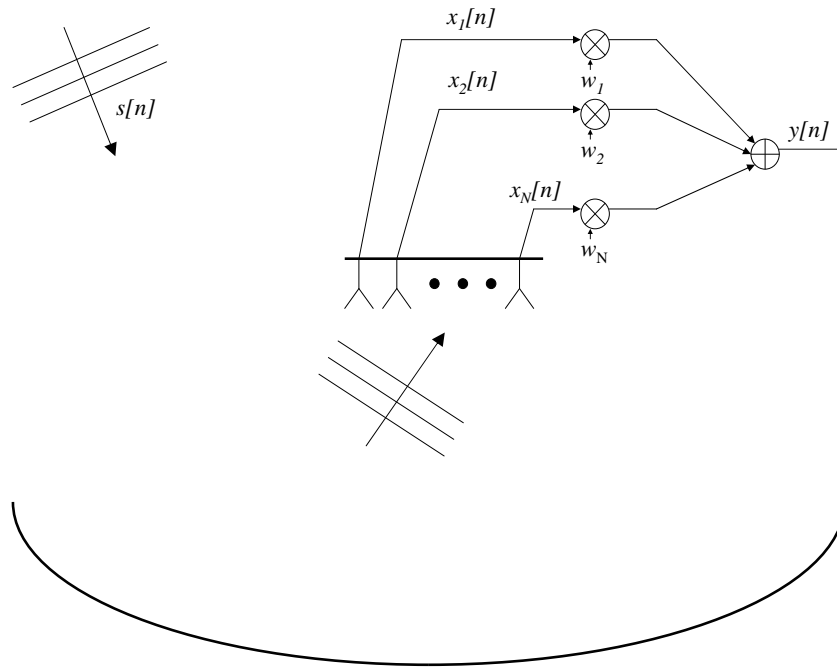


Figure 4.8: Beamformer for a reflector antenna with a phased array feed. $x_i[n]$ are the different time samples of the signal $s[n]$ taken at each feed element.

Only limited work has been done on the use of array feeds in radio astronomy. For this reason we first sought to determine the attainable sensitivity of an array feed with no interferer present, relative to the baseline sensitivity of a standard waveguide feed. Several different optimization algorithms were implemented to maximize sensitivity. These algorithms all produced the same maximum sensitivity, but a line-search algorithm proved to be the fastest and was used in all of the maximum sensitivity calculations.

The maximum sensitivity calculations were also compared to the results obtained using the conjugate field match (CFM) method. It has been shown that this technique very closely approximates the maximum gain of an array feed if the spacing of the elements is greater than $.5\lambda$ [46]. This method entails sampling the electric field in the plane of the array due to a plane wave from a given source direction. The conjugate of these samples are the weights for the array elements. The CFM weights

can also be obtained if the exact beam response (magnitude and phase) of each array element is known. The weights are simply the conjugate of the steering vector in the direction of interest. In simulation, this method is easier because the beam responses are known. This method, however, is more difficult in practice because on a large reflector the exact beam response of the array plus reflector is difficult to measure and calibrate far from the boresight direction.

The first simulation involved finding in which vertical plane the array would produce the highest sensitivity. Figure 4.9 shows the maximum sensitivity of the 7-element array and reflector as a function of vertical offset distance relative to the focal plane. Figures 4.10 and 4.11 show the gain and spillover efficiency of the array using the same weights. The highest sensitivity is achieved at the focal plane, although we note that only a small offset is required before the array is smaller than the geometrical optics cone of the fields focused by the reflector.

The array feed also attains a higher sensitivity than the waveguide feed. As with the waveguide feed, optimizing sensitivity entails sacrificing gain in order to achieve higher spillover efficiency. In Figure 4.10 the gain of the array is 2 dB below that achieved using the CFM method, but the array has higher spillover efficiency (see Figure 4.11) and thus higher sensitivity. The CFM has very low spillover efficiency because it is used only to optimize gain. The array pattern on the reflector dish can be seen in Figure 4.12. It is compared to the pattern produced from the waveguide feed. The optimal pattern would be a rect shape on the dish. This would produce 100% spillover efficiency and the highest gain possible, but could only be achieved with an infinite array. As the array size increases, the optimized pattern on the dish would look more and more like a rect. The limiting sensitivity is $.024 \text{ Jy}^{-1}$ (see Figure 5.9).

4.8 Beamscanning

In a traditional radio astronomy receiver, it is possible to perform beamscanning by displacing the feed in a lateral direction. This can be seen in Figure 4.13.

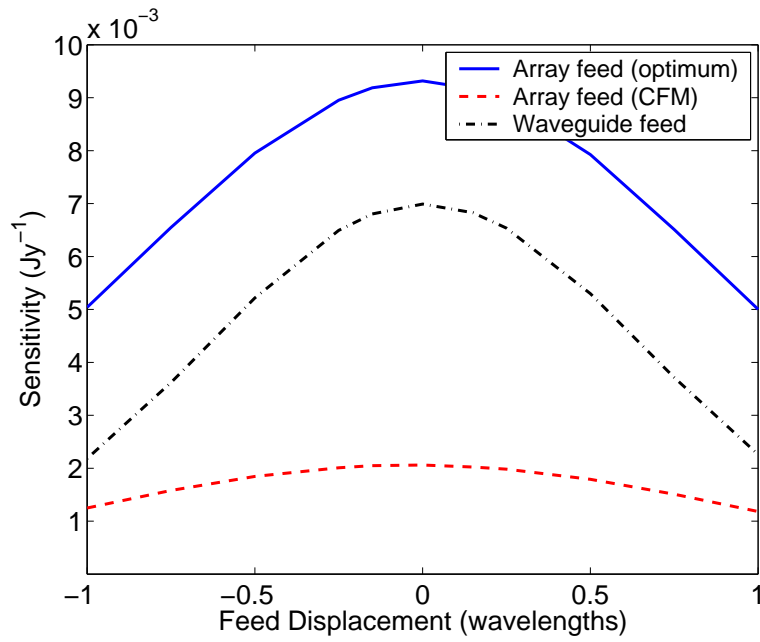


Figure 4.9: Sensitivity vs. feed displacement from the focal plane. The array feed consists of a 7 element dipole hex array.

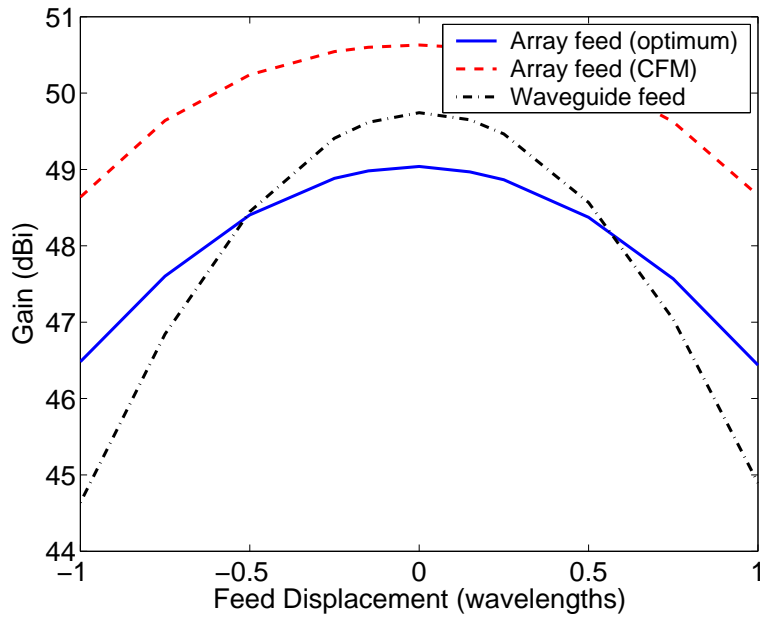


Figure 4.10: Gain of array using the maximum sensitivity weights from Figure 4.9 compared to the array feed using the CFM weights and a standard waveguide feed.

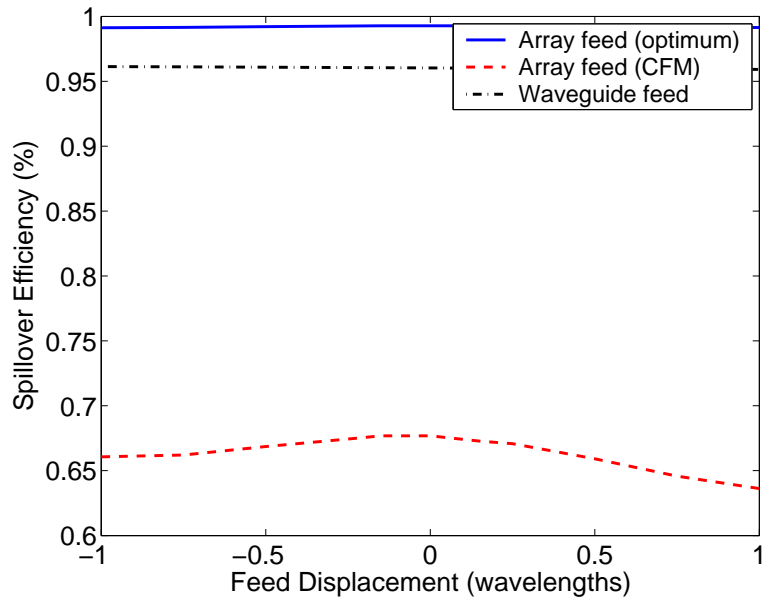


Figure 4.11: Spillover efficiency using the maximum sensitivity weights from Figure 4.9 compared to the array feed using the CFM weights and a standard waveguide feed.

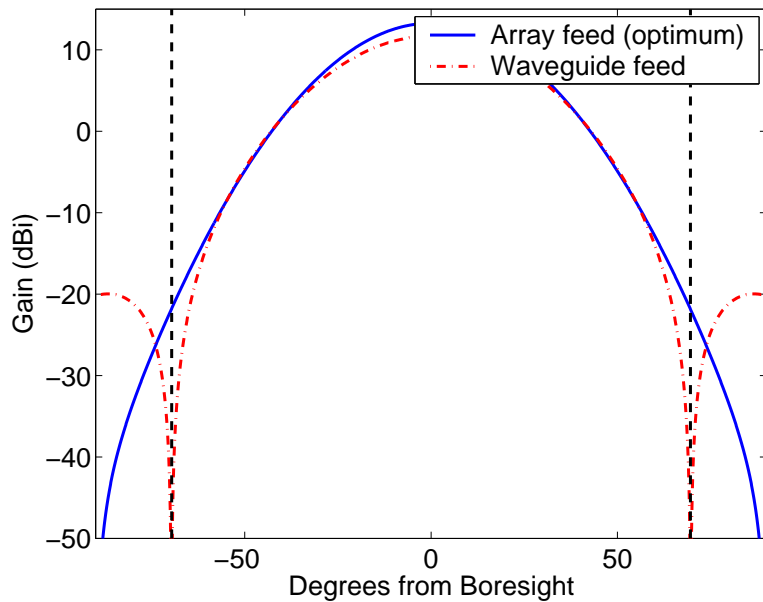


Figure 4.12: Optimized array pattern on the reflector dish compared to the waveguide feed pattern. The vertical line is the location of the reflector dish edge.

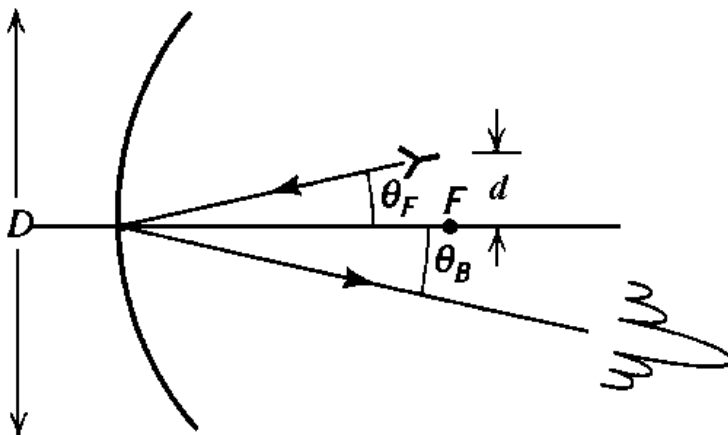


Figure 4.13: Beam scanning of a reflector antenna by feed displacement (Figure used from [47]).

Beams scanning can be quantified by using the beam deviation factor (BDF) [47] defined as:

$$\text{BDF} = \frac{\theta_B}{\theta_F} \quad (4.27)$$

where θ_B is the angle from the focal point to the main beam and θ_F is the angle from the focal point to the feed element as shown in Figure 4.13. For small lateral displacements the following approximate expression can be used,

$$\text{BDF} = \frac{1 + 0.36[4\frac{F}{D}]^{-2}}{1 + [4\frac{F}{D}]^{-2}} \quad (4.28)$$

where F is the focal length and D is the diameter of the reflector dish. The lateral displacement needed to achieve the desired scan angle θ_B can then be found from

$$d = F \tan(\theta_B) . \quad (4.29)$$

For beams scanning applications, a key question is how far a single beam can be steered while still maintaining high sensitivity with a phased array feed. This result can be seen in Figure 4.14, for arrays at several offset distances relative to the focal plane. The waveguide feed results are obtained by moving the feed in a lateral direction in the focal plane such that its main beam is at the desired scan angle as described

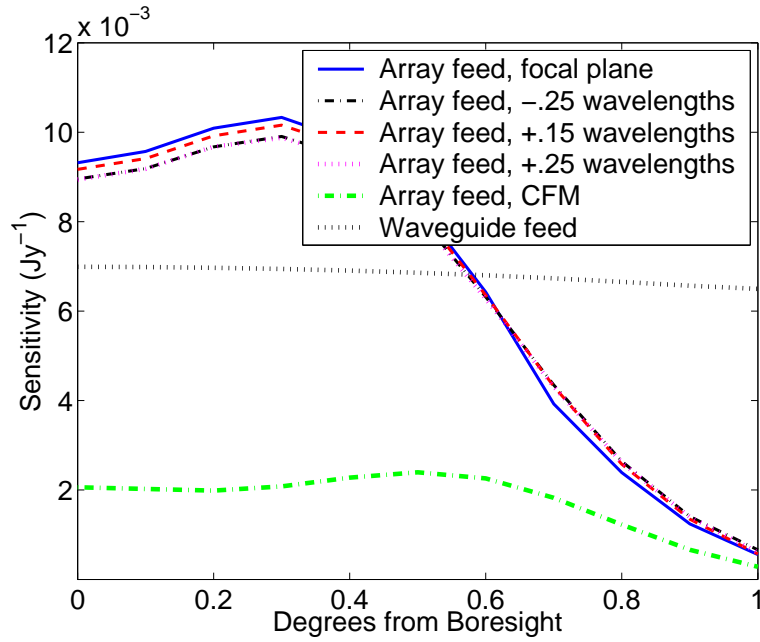


Figure 4.14: Sensitivity as a function of steered beam angle.

above. Figures 4.15 and 4.16 show the gain and spillover efficiency corresponding to the weights used in Figure 4.14. The array in the focal plane produces the highest sensitivity, even for the steered beams. The beam is scanned along the θ -direction with $\phi = 0^\circ$. Along this direction the symmetry properties of the array can be utilized so that each individual element does not need to be optimized. Normally, 6 complex weights need to be optimized, corresponding to the outer 6 elements of the array referenced to the center element. By using the symmetry, only 4 are needed. This makes the optimization procedure much quicker.

The sensitivity in Figure 4.14 increases slightly from 0° to $.3^\circ$. The reason for this increase can be seen from Figure 4.17. Figure 4.17(a) is a plot of the focal field distribution due to an arriving plane wave from the boresight direction. The black dots in the plot are the locations of the dipole elements. The majority of the power is received by the center element. Figure 4.17(b) shows the focal field distribution when the plane wave is arriving at an angle of 0.3° from boresight. Most of the power

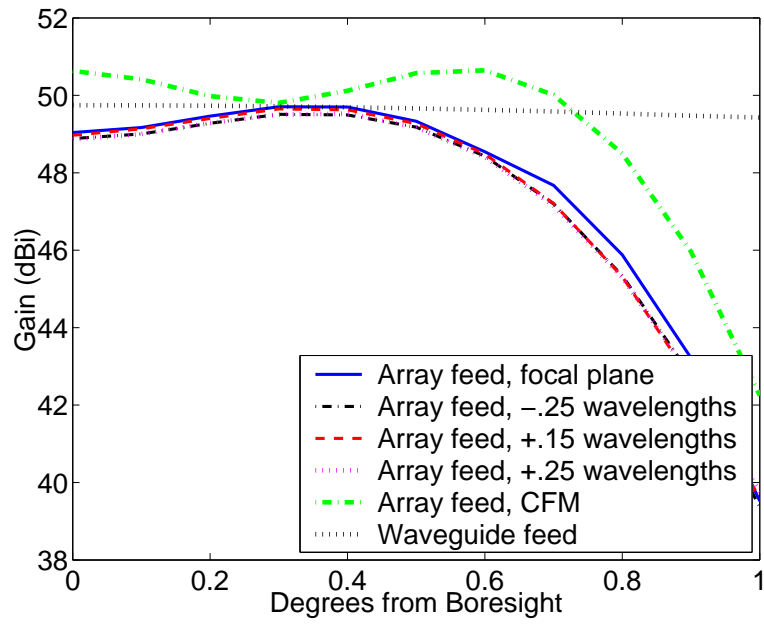


Figure 4.15: Gain of array using the maximum sensitivity weights from Figure 4.14.

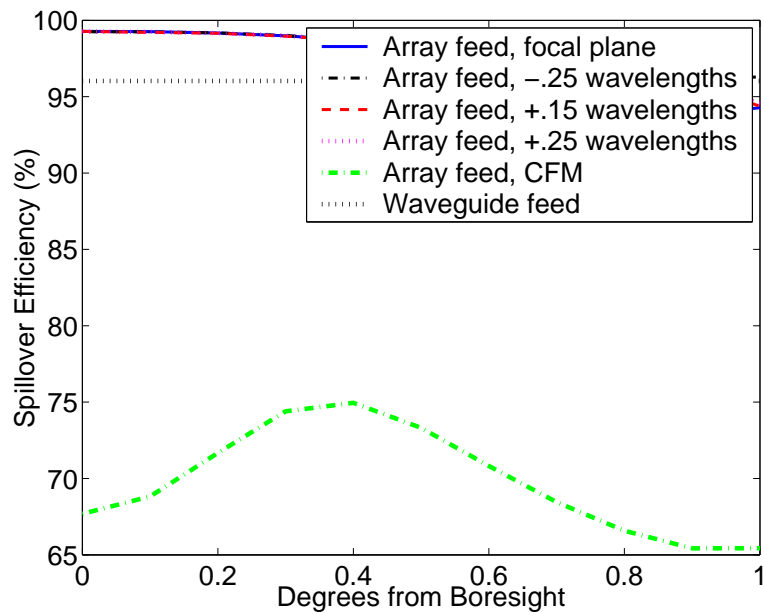
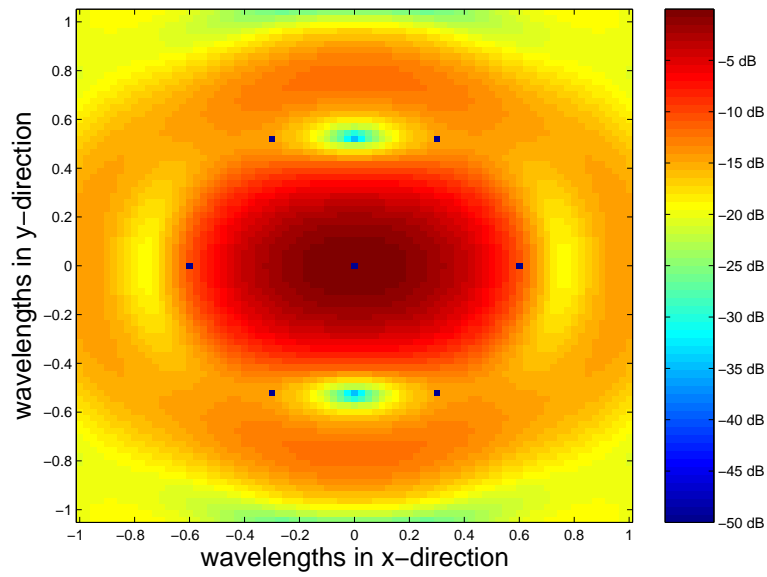


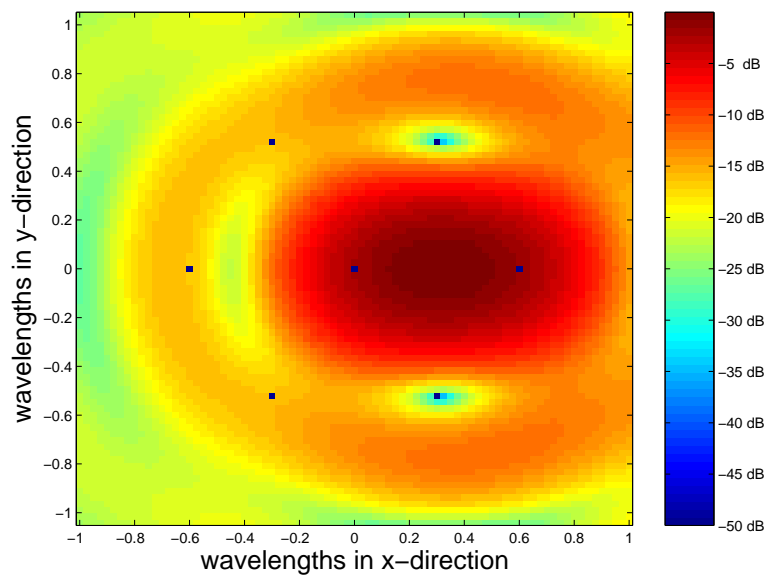
Figure 4.16: Spillover efficiency using the maximum sensitivity weights from Figure 4.14.

is received by two elements instead of one which increases the gain of the antenna slightly.

Since the beams are all steered electronically it is possible to form multiple beams simultaneously, but it was not known whether the beams would all have high sensitivity. If they could, radio astronomers would be able to do rapid sky surveys by being able to look in several observation directions at the same time. This significantly reduces observation times where normally the reflector antenna would need to be repositioned at every observation direction. There is no limit to the number of beams that can be formed. Figures 4.18 and 4.19 show a simulation of 7 high sensitivity beams. Figure 4.18 is a ϕ -cut at $\theta = .3^\circ$. It is a plot of the gain patterns of the 6 outer beams. Figure 4.19 is a θ -cut through each of the 6 outer beams. When forming multiple beams for radio astronomy purposes, it is desirable to have the maximum gain of each beam meet at the 3 dB point of the nearest beams. These beams very closely meet this requirement. The sensitivity of the beams can be seen in Figure 4.20. All 7 beams have high sensitivity.



(a)



(b)

Figure 4.17: (a) Focal field distribution of incoming plane wave in boresight direction. The axes are in wavelengths from the focal point and the color scale is in dB referenced to the main signal. (b) Focal field distribution of incoming plane wave $.3^\circ$ from boresight direction.

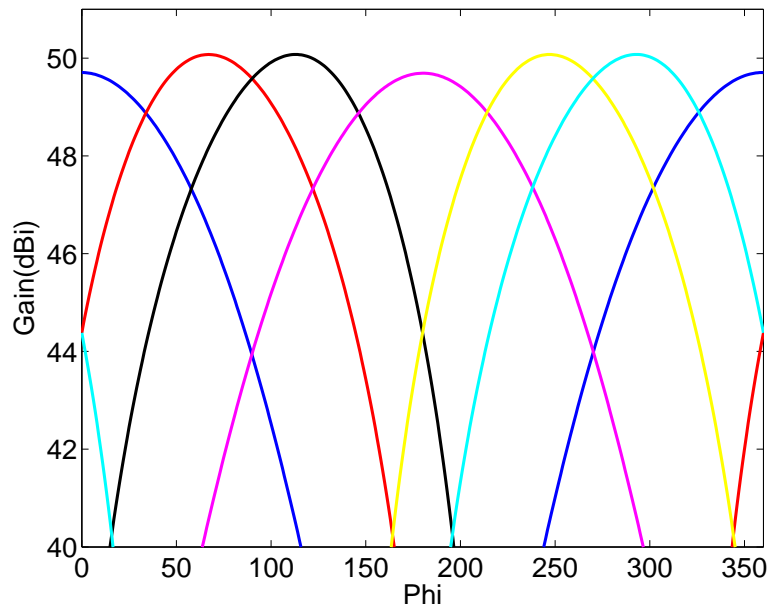


Figure 4.18: Beam patterns of 6 outer beams. The plot is a ϕ -cut at $\theta = .3^\circ$.

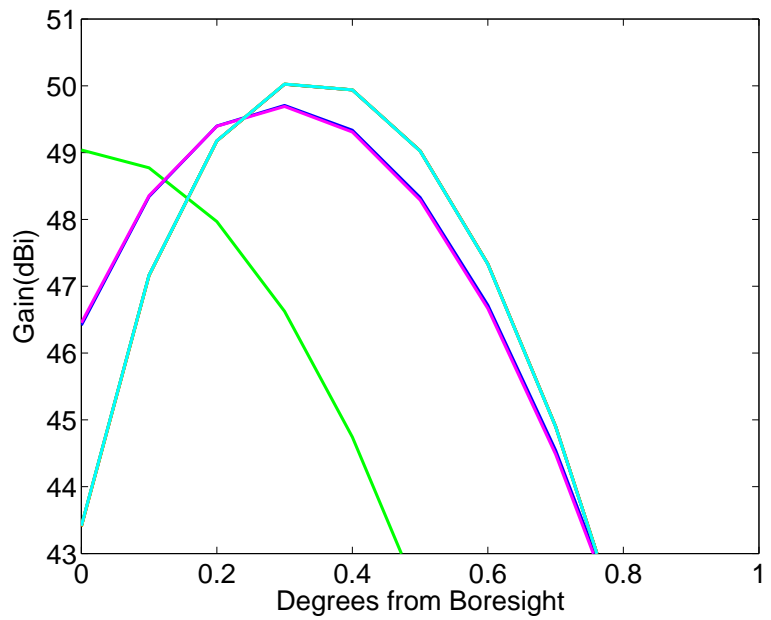


Figure 4.19: Beam patterns of 7 beams. The plot is a θ -cut through each of the 6 outer beams.

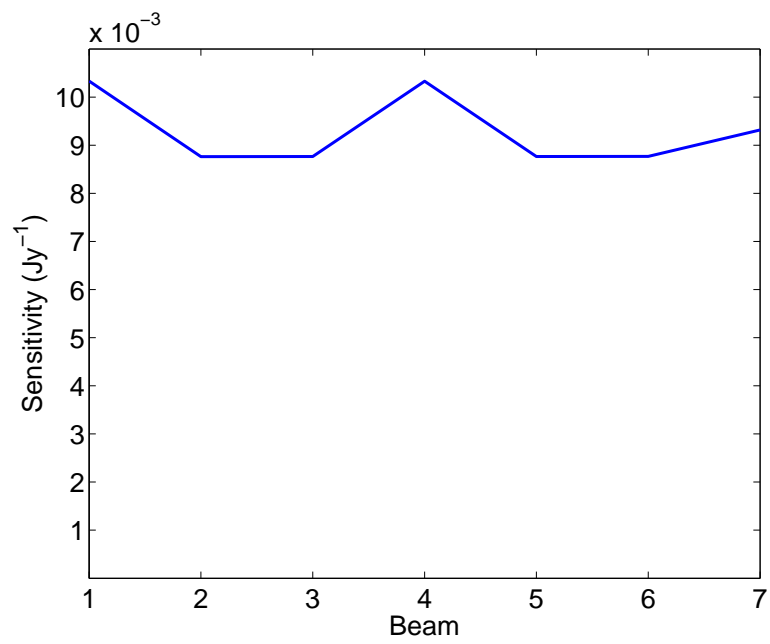


Figure 4.20: The sensitivity of each of the 7 beams. Beam 7 is the center beam.

Chapter 5

RFI Mitigation using Phased Array Feed

5.1 Maximum SNR and LCMV

RFI mitigation is the primary goal in the design and implementation of the phased array feed. It is important to know if interference mitigation can be achieved while still maintaining high sensitivity. For this reason a new definition of sensitivity was needed. When an interferer is present its noise temperature will decrease the sensitivity of the measurement. We define effective sensitivity in the presence of RFI as

$$S_{eff}(1/\text{Jy}) = \frac{G(\text{K}/\text{Jy})}{T_{sys}(\text{K}) + T_{int}(\text{K})} \quad (5.1)$$

which differs from sensitivity as usually defined in that interference power is included in the noise temperature. This quantity is essentially SNR at the receiver output for a unit intensity signal (1 Jy).

Two models were also needed in order to effectively study interference mitigation. The first was a model for the interference. We chose a GLONASS-type signal at 1612 MHz. An appropriate noise model was also needed. The spillover noise was assumed to arrive at the feed from a warm 300 K background over the solid angle extending in elevation angle from the reflector rim to the focal plane. The details of this model can be found in Appendix B. The noise model makes the assumption that the array elements are isotropic radiators. It will be shown that this simplification has little effect on RFI mitigation (see Figure 5.6).

There are several different beamforming algorithms that could be used with a phased array feed. We chose to use maximum SNR. The weights are chosen to

directly maximize the signal-to-noise ratio, which is equivalent to maximizing sensitivity. This results in the highest possible sensitivity that can be achieved for a given array configuration. The criterion is

$$\max_{\mathbf{w}} \frac{\mathbf{w}^H \mathbf{R}_{ss} \mathbf{w}}{\mathbf{w}^H \mathbf{R}_{NN} \mathbf{w}} \quad (5.2)$$

where

$$\mathbf{R}_{ss} = E[\mathbf{x}_s \mathbf{x}_s^H] \quad (5.3)$$

and

$$\mathbf{R}_{NN} = \mathbf{R}_{nn} + \mathbf{R}_{ii} . \quad (5.4)$$

\mathbf{R}_{nn} is the noise correlation matrix due to the spillover and LNA noise as defined in Appendix B. \mathbf{x}_s is a vector containing the time samples at the array elements due to the signal. \mathbf{R}_{ii} is the correlation matrix due to the interference. The solution is

$$\mathbf{R}_{NN}^{-1} \mathbf{R}_{ss} \mathbf{w} = \lambda_{\max} \mathbf{w} . \quad (5.5)$$

The solution is the eigenvector corresponding to the largest eigenvalue of $\mathbf{R}_{NN}^{-1} \mathbf{R}_{ss}$. One drawback to max SNR is that the covariance matrices of the desired signal, \mathbf{R}_{ss} and the noise, \mathbf{R}_{NN} must be known.

Another useful algorithm is linearly constrained minimum variance (LCMV). LCMV works by placing constraints on the beamformer response such that the signals from the direction of interest are passed with a desired gain and phase [48]. LCMV also minimizes the output variance subject to the response constraint. This means that the desired signal is preserved while the variance due to interfering signals or noise are minimized. The method for choosing the weights is written as

$$\min_{\mathbf{w}} \mathbf{w}^H \mathbf{R}_{xx} \mathbf{w} \quad \text{subject to} \quad \mathbf{C}^H \mathbf{w} = \mathbf{f} \quad (5.6)$$

where \mathbf{C}^H is a list of steering vectors ($\mathbf{d}^H(\theta, \phi)$) in directions $\theta_1, \phi_1 \dots \theta_N, \phi_N$. \mathbf{f} is a vector of constraints corresponding to the desired gain in the directions $\theta_1, \phi_1 \dots \theta_N, \phi_N$. If the signal, interference, and noise are uncorrelated with respect to each other, \mathbf{R}_{xx} is defined as

$$\mathbf{R}_{xx} = \mathbf{R}_{ss} + \mathbf{R}_{NN} . \quad (5.7)$$

The solution to Eq. 5.6 is

$$\mathbf{w} = \mathbf{R}_{xx}^{-1} \mathbf{C} [\mathbf{C}^H \mathbf{R}_{xx}^{-1} \mathbf{C}]^{-1} \mathbf{f} . \quad (5.8)$$

For our purposes, there is only one constraint in the direction of the signal of interest. In most radio astronomy receivers the exact beam response (gain and phase) is not known far from the boresight direction, so a constraint cannot be placed in the direction of the interferer even if this direction is known.

It can be shown that the weights corresponding to LCMV and max SNR are equal under the assumptions of the signal component being narrowband and only one constraint being used in LCMV. If the signal component is narrowband, then

$$\mathbf{R}_{ss} = \sigma_s^2 \mathbf{d}(\theta, \phi) \mathbf{d}^H(\theta, \phi) . \quad (5.9)$$

In this case the max SNR weights can be found from Eq. 5.5 to be

$$\mathbf{w} = \frac{\mathbf{R}_{NN}^{-1} \sigma_s^2 \mathbf{d} \mathbf{d}^H \mathbf{w}}{\lambda_{\max}} . \quad (5.10)$$

Since

$$\alpha_1 = \frac{\sigma_s^2 \mathbf{d}^H \mathbf{w}}{\lambda_{\max}}$$

is a complex constant, the solution is

$$\mathbf{w} = \alpha_1 \mathbf{R}_{NN}^{-1} \mathbf{d} . \quad (5.11)$$

In the case of a single constraint the LCMV solution is

$$\mathbf{w} = \mathbf{R}_{xx}^{-1} \mathbf{d} [\mathbf{d}^H \mathbf{R}_{xx}^{-1} \mathbf{d}]^{-1} \mathbf{f} \quad (5.12)$$

where

$$\mathbf{R}_{xx} = \mathbf{R}_{ss} + \mathbf{R}_{NN} \quad (5.13)$$

$$\mathbf{R}_{ss} = \sigma_s^2 \mathbf{d} \mathbf{d}^H \quad (5.14)$$

and since

$$\alpha_2 = [\mathbf{d}^H \mathbf{R}_{xx}^{-1} \mathbf{d}]^{-1} \mathbf{f}$$

is a complex constant, the solution can be written as

$$\mathbf{w} = \alpha_2 (\mathbf{R}_{NN} + \sigma_s^2 \mathbf{d} \mathbf{d}^H)^{-1} \mathbf{d} . \quad (5.15)$$

By applying the matrix inversion lemma, this equation becomes

$$\mathbf{w} = \alpha_2 \left[\mathbf{R}_{NN}^{-1} - \frac{\sigma_s^2 (\mathbf{R}_{NN}^{-1} \mathbf{d}) (\mathbf{d}^H \mathbf{R}_{NN}^{-1})}{1 + \mathbf{d}^H \mathbf{R}_{NN}^{-1} \mathbf{d}} \right] \mathbf{d} \quad (5.16)$$

$$= \alpha_2 \left[1 - \frac{\sigma_s^2 \mathbf{d}^H \mathbf{R}_{NN}^{-1} \mathbf{d}}{1 + \mathbf{d}^H \mathbf{R}_{NN}^{-1} \mathbf{d}} \right] \mathbf{R}_{NN}^{-1} \mathbf{d} . \quad (5.17)$$

The expression in brackets is another complex constant, so if we let

$$\alpha_3 = \alpha_2 \left[1 - \frac{\sigma_s^2 \mathbf{d}^H \mathbf{R}_{NN}^{-1} \mathbf{d}}{1 + \mathbf{d}^H \mathbf{R}_{NN}^{-1} \mathbf{d}} \right]$$

the solution is

$$\mathbf{w} = \alpha_3 \mathbf{R}_{NN}^{-1} \mathbf{d} . \quad (5.18)$$

It can be seen that Eqs. 5.11 and 5.18 only differ by a complex constant. Thus the weights provided by the LCMV and max SNR algorithms are equivalent and both produce the same gain, spillover efficiency, and maximum sensitivity.

Using these spatial filtering algorithms, beamformer array weights were designed to steer the main beam to the boresight direction and suppress a RFI signal. Figure 5.1 shows the final beam pattern for the center beam with the interferer at 30° with an interference-to-noise ratio (INR) of 0 dB at the center feed element. Figure 5.2 shows a detail of the null placed in the direction of the interferer. In order to place the null some gain and spillover efficiency is lost. The overall sensitivity drops by only 0.8 dB from the maximum possible sensitivity. The effective sensitivity is stable in the limits of large and small interferer powers, as shown in Figure 5.3. The array is compared to a waveguide feed for which the effective sensitivity decreases dramatically as the interference power increases.

Although the algorithms are able to suppress RFI, some beam shape distortion occurs, as shown in Figure 5.4. The maximum gain is shifted slightly from 0°. The sidelobes also increase a few dB when using LCMV and an interferer is present. More advanced algorithms with shape tolerance constraints are required to eliminate this

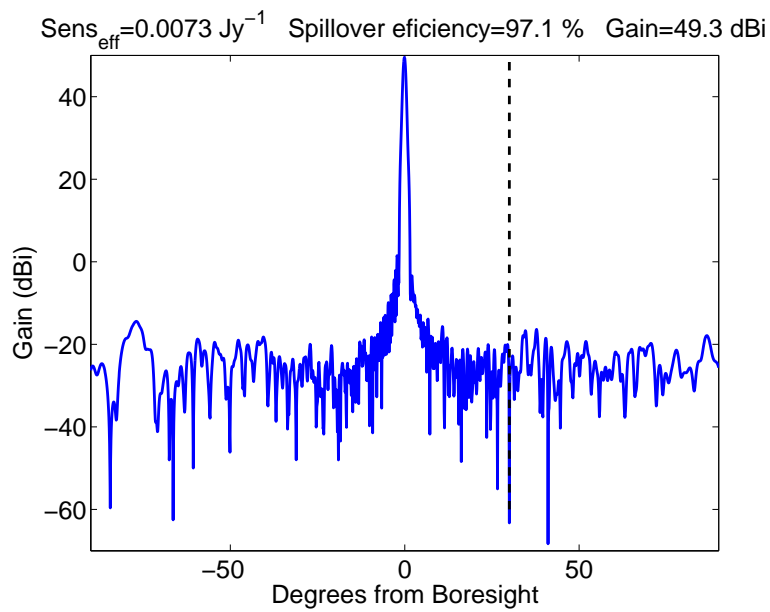


Figure 5.1: Beam pattern using max SNR/LCMV to cancel interferer at 30°. The INR is 0 dB at the input to the center element.

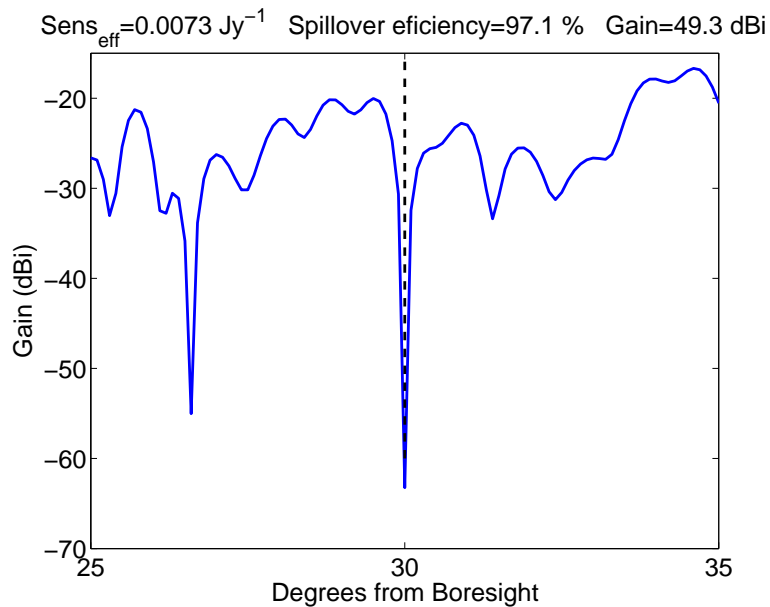


Figure 5.2: Detail of null in the direction of the interferer.

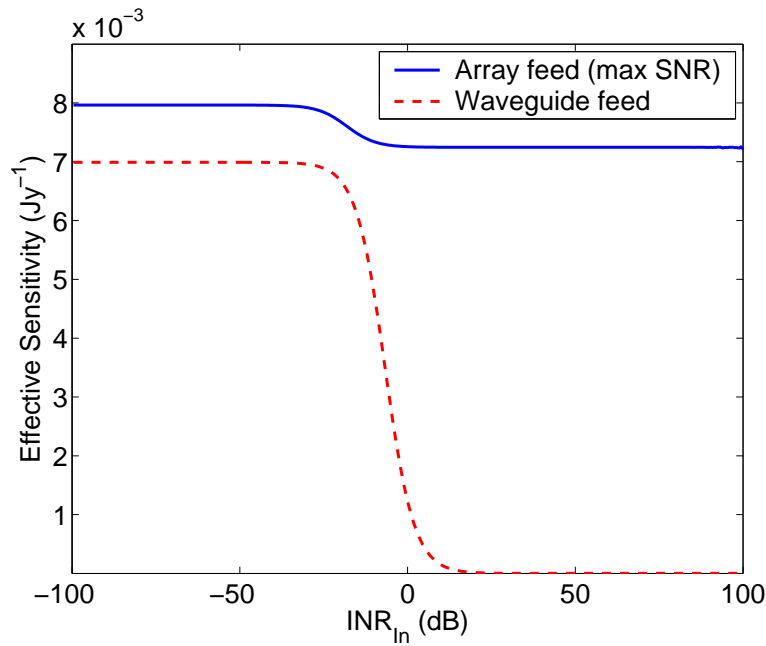


Figure 5.3: Effective sensitivity vs. INR at the the center feed element for the phased array using max SNR. For comparison the effective sensitivity of a standard waveguide feed is shown.

problem. More significantly, the effective sensitivity is not robust relative to interferer angle of arrival. Figure 5.5 shows that at some angles high effective sensitivity cannot be achieved. In these cases, the center element has a large response in the direction of the interferer, so that the outer elements must be weighted larger in order to combine the element signals in such a way that the interference is cancelled. This decreases the overall antenna gain and increases the spillover noise. It is possible to reduce this drop in effective sensitivity if a larger array is used, as demonstrated in the following section.

It is important to note that these results are general with respect to the choice of beamformer algorithm in that for the signal and noise models considered here (maximum SNR and LCMV) both lead to optimal sensitivity. To test this, the moving interferer scenario was processed using the sensitivity optimizer instead of max SNR. Figure 5.6 shows the maximum possible sensitivity in the presence of the

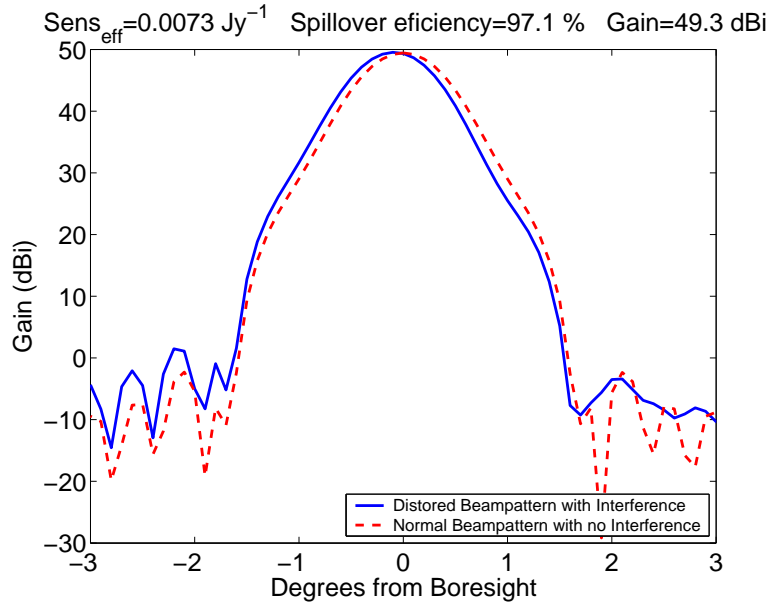


Figure 5.4: Distorted beam pattern of the phased array feed using max SNR. Maximum gain is shifted slightly from 0° .

interferer along with the max SNR results. The optimized sensitivity results are slightly higher due to the noise model we used. If an exact noise model were used max SNR would produce the same results. It is also important to note that the decrease in effective sensitivity is not due to the interference power, but the decrease in gain and spillover efficiency. The algorithm is able to reject most of the interferer power for all angles. In Figure 5.7 the conventional sensitivity (see Eq. 2.1) is only slightly higher than effective sensitivity meaning that very little interference power is being received. Figure 5.8 shows a plot of the interference rejection achieved with max SNR. Interference rejection is the amount of attenuation the interferer power receives. Although the interference rejection varies, the rejection is at least 20 dB for almost all interferer arrival angles. These results show that the array itself must be modified or increased in size in order to improve the sensitivity results. It should be noted that all of these tests were also run with an array displaced up to 1.0 wavelengths in the vertical direction, but the focal plane array provided the best interference mitigation.

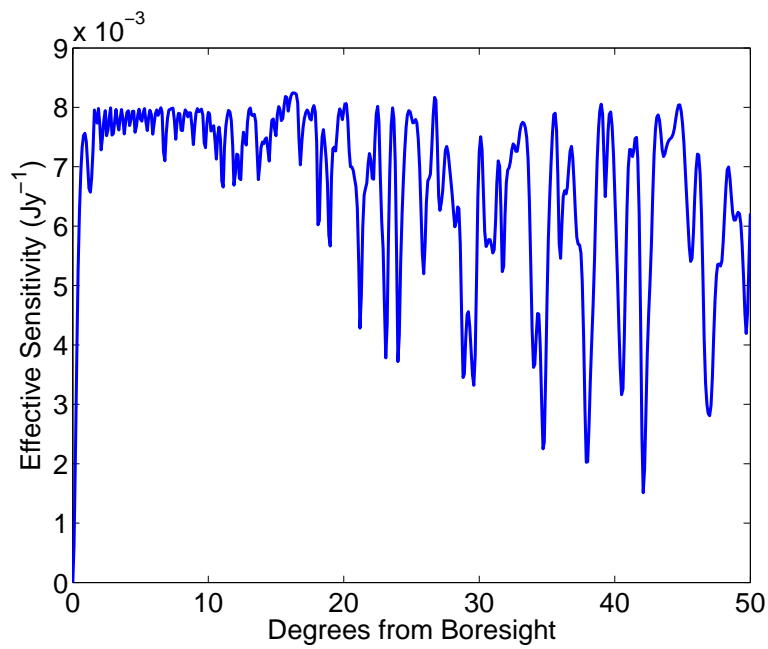


Figure 5.5: Effective sensitivity as a function of interferer location using max SNR.

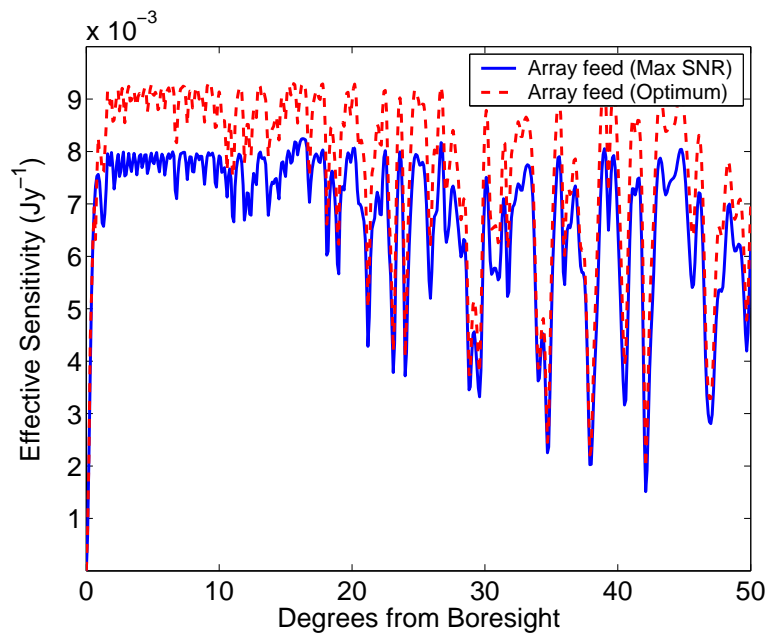


Figure 5.6: Optimum effective sensitivity using a numerical search algorithm compared to max SNR effective sensitivity.

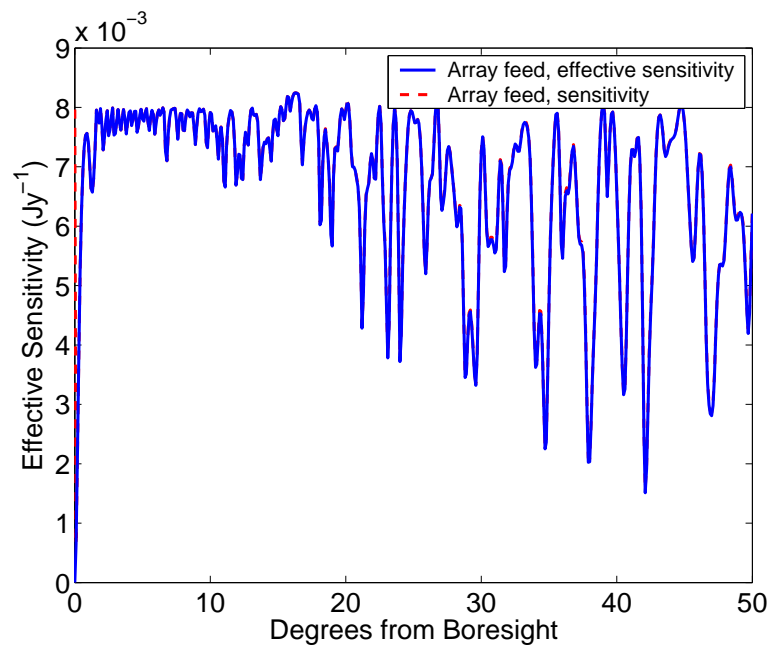


Figure 5.7: Effective sensitivity compared to basic sensitivity definition, which does not include interferer power.

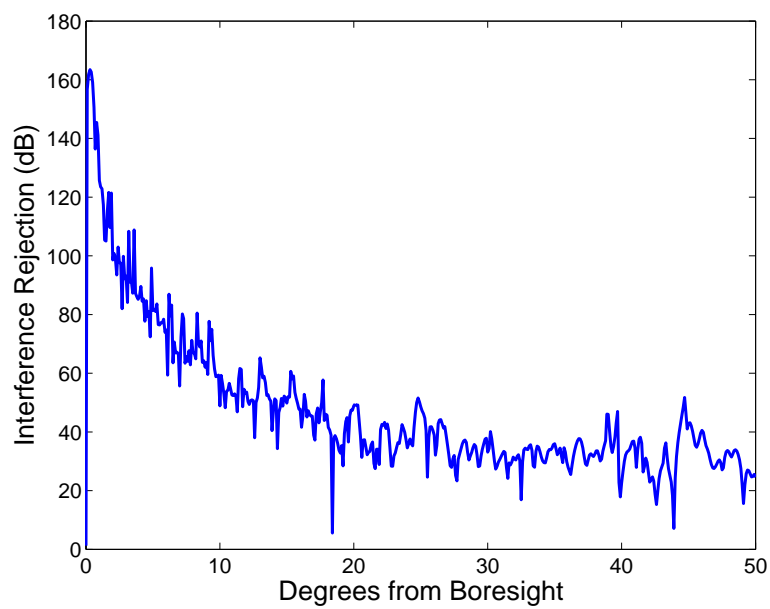


Figure 5.8: Interference rejection as a function of interferer location using max SNR.

5.2 Maximum SNR Using 19-element Array

It was thought that one way to overcome some of the problems encountered using max SNR on the 7-element array could be overcome by using a larger array. This would provide more degrees of freedom and allow the beamformer to produce higher gain and higher spillover efficiency. A 19-element hexagonal array was simulated using GRASP8. Max SNR was used on the phased array feed and compared to the results produced with the 7-element array. Figure 5.9 shows how the two arrays compared. The theoretical maximum sensitivity is also shown on the plot. This maximum means the aperture efficiency and spillover efficiency are 100 percent, so that the only noise component entering the system is the noise due to the receivers. With only two exceptions at 35° and 42° , the 19-element array is able to produce a higher effective sensitivity than the 7-element array can produce for any interferer arrival angle. The effective sensitivity variance of the 19-element array is less, but there are still locations where high sensitivity cannot be achieved. However, at these locations the effective sensitivity only drops by approximately 3 dB on the larger array feed.

An analysis of the low sensitivity points was performed on the 19-element array. As with the 7-element array, the outer element weights had higher amplitudes at these locations. The INR at the input to the center element is high at these locations as well. This can be seen by comparing Figures 5.10(a) and 5.10(b). The dashed lines represent the locations of lower effective sensitivity. The rapid variations in the INR at the center element are due to its gain pattern structure in the sidelobes. The outer weights are used more to compensate for the high interference power received at the center element, which rejects the interference power but also lowers the gain and spillover efficiency. Figure 5.11 and 5.12 show the gain and spillover efficiency of the 19-element array which correspond to effective sensitivity in Figure 5.9. These plots show that both gain and spillover efficiency loss are responsible for the drop in effective sensitivity. Simulations were also ran with the 19-element array placed in different vertical planes. Once again, the focal plane array produced the highest effective sensitivity.

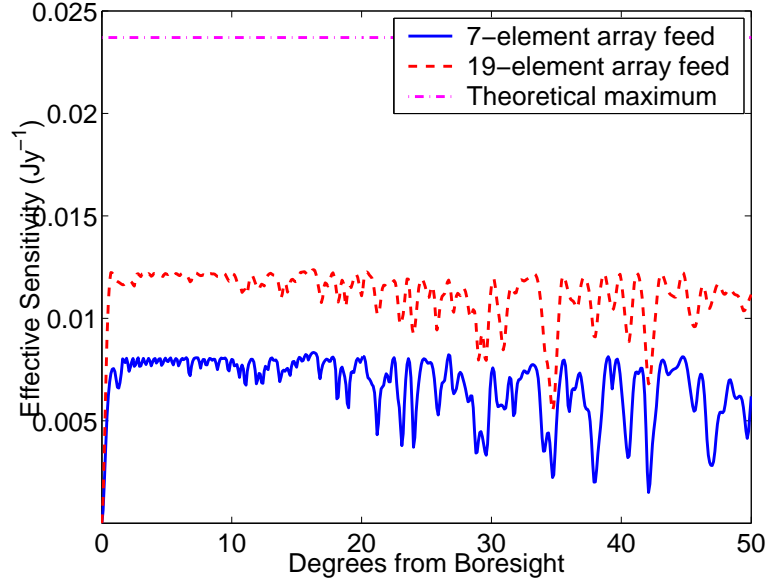


Figure 5.9: Effective sensitivity vs. interferer arrival angle for the 19 and 7 element phased array feeds using max SNR. The theoretical maximum sensitivity for a rect illumination pattern is also shown.

5.3 Analysis of SNR Behavior

It was desired to further understand the physical meaning of the drop in sensitivity at certain interferer arrival angles. This lead to an analysis of the maximum SNR analytical solution. The SNR of the array feed is given by

$$\text{SNR} = \frac{\mathbf{w}^H \mathbf{R}_{ss} \mathbf{w}}{\mathbf{w}^H \mathbf{R}_{NN} \mathbf{w}} \quad (5.19)$$

where

$$\mathbf{R}_{NN} = \mathbf{R}_{nn} + \mathbf{R}_{ii} \quad (5.20)$$

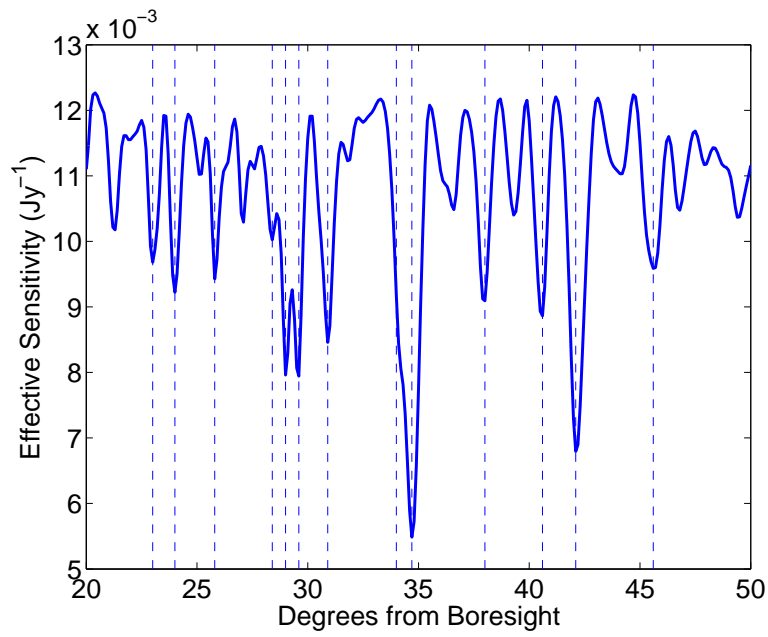
$$\mathbf{R}_{ii} = \sigma_i^2 \mathbf{d}_i \mathbf{d}_i^H \quad (5.21)$$

$$\mathbf{R}_{ss} = \sigma_s^2 \mathbf{d}_s \mathbf{d}_s^H \quad (5.22)$$

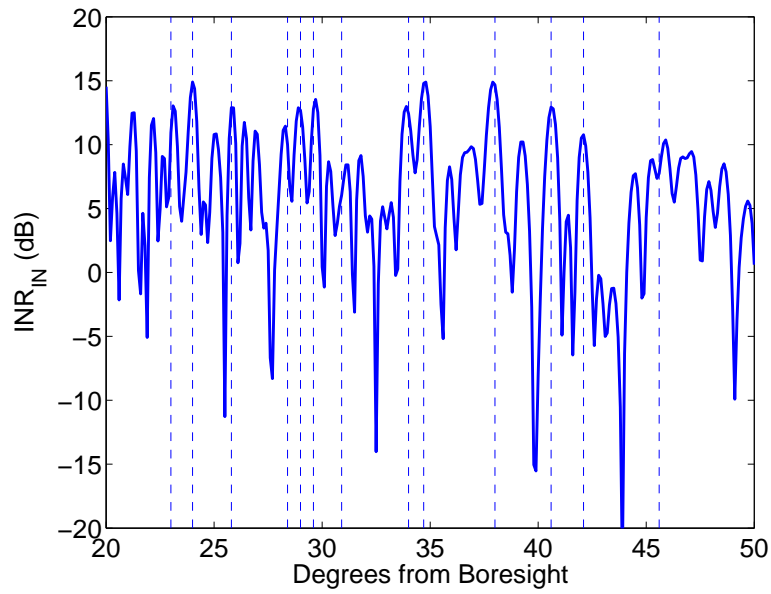
and

$$\mathbf{w} = \alpha_1 \mathbf{R}_{nn}^{-1} \mathbf{d} \quad (5.23)$$

as defined in Eq. 5.11. \mathbf{R}_{nn} is the noise correlation matrix due to the spillover noise and LNA noise as defined in Appendix B. With these parameters the SNR expression



(a)



(b)

Figure 5.10: (a) The effective sensitivity of the 19-element array feed vs. interferer arrival angle using max SNR. The dashed lines are placed at interferer arrival angles where the effective sensitivity is below 0.01 Jy^{-1} . (b) The INR at the input to the center element vs. interferer arrival angle.

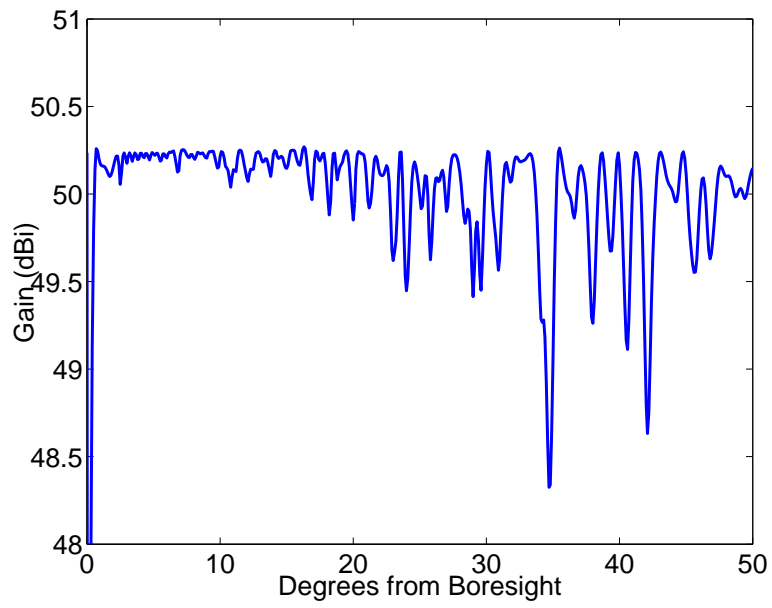


Figure 5.11: The gain of the 19-element array feed vs. interferer arrival angle using the max SNR algorithm.

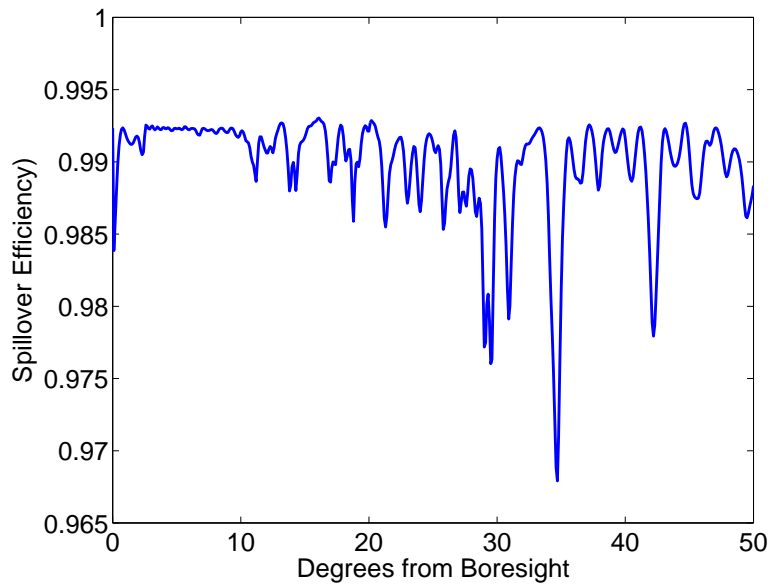


Figure 5.12: The spillover efficiency of the 19-element array feed vs. interferer arrival angle using the max SNR algorithm.

can be simplified to

$$\text{SNR} = \frac{\mathbf{w}^H (\sigma_s^2 \mathbf{d}_s \mathbf{d}_s^H) \mathbf{w}}{\mathbf{w}^H \mathbf{R}_{NN} \mathbf{w}} \quad (5.24)$$

$$= \frac{\sigma_s^2 (\mathbf{w}^H \mathbf{d}_s) (\mathbf{d}_s^H \mathbf{w})}{\mathbf{w}^H \mathbf{d}_s} \quad (5.25)$$

$$= \sigma_s^2 \mathbf{d}_s^H \mathbf{w} . \quad (5.26)$$

Using the matrix inversion lemma \mathbf{R}_{NN}^{-1} can be found,

$$\mathbf{R}_{NN}^{-1} = (\mathbf{R}_{nn} + \sigma_i^2 \mathbf{d}_i \mathbf{d}_i^H)^{-1} \quad (5.27)$$

$$= \mathbf{R}_{nn}^{-1} - \frac{\sigma_i^2 (\mathbf{R}_{nn}^{-1} \mathbf{d}_i) (\mathbf{d}_i^H \mathbf{R}_{nn}^{-1})}{1 + \sigma_i^2 \mathbf{d}_i^H \mathbf{R}_{nn}^{-1} \mathbf{d}_i} \quad (5.28)$$

and

$$\mathbf{w} = \mathbf{R}_{nn}^{-1} \mathbf{d}_s - \frac{\sigma_i^2 \mathbf{R}_{nn}^{-1} \mathbf{d}_i \mathbf{d}_i^H \mathbf{R}_{nn}^{-1} \mathbf{d}_s}{1 + \sigma_i^2 \mathbf{d}_i^H \mathbf{R}_{nn}^{-1} \mathbf{d}_i} . \quad (5.29)$$

From Eq. 5.26

$$\text{SNR} = \sigma_s^2 \mathbf{d}_s^H \left[\mathbf{R}_{nn}^{-1} \mathbf{d}_s - \frac{\sigma_i^2 \mathbf{R}_{nn}^{-1} \mathbf{d}_i \mathbf{d}_i^H \mathbf{R}_{nn}^{-1} \mathbf{d}_s}{1 + \sigma_i^2 \mathbf{d}_i^H \mathbf{R}_{nn}^{-1} \mathbf{d}_i} \right] . \quad (5.30)$$

In Eq. 5.30, it can be seen that SNR is composed of two parts. The first component is the SNR if there is no interference present,

$$\text{SNR}_{no \ int} = \sigma_s^2 \mathbf{d}_s^H \mathbf{R}_{nn}^{-1} \mathbf{d}_s . \quad (5.31)$$

The second component is the degradation of SNR due to the interference,

$$\Delta \text{SNR} = -\sigma_s^2 \sigma_i^2 \frac{\mathbf{d}_s^H \mathbf{R}_{nn}^{-1} \mathbf{d}_i \mathbf{d}_i^H \mathbf{R}_{nn}^{-1} \mathbf{d}_s}{1 + \sigma_i^2 \mathbf{d}_i^H \mathbf{R}_{nn}^{-1} \mathbf{d}_i} \quad (5.32)$$

$$= -\sigma_s^2 \sigma_i^2 \frac{|\mathbf{d}_s^H \mathbf{R}_{nn}^{-1} \mathbf{d}_i|^2}{1 + \sigma_i^2 \mathbf{d}_i^H \mathbf{R}_{nn}^{-1} \mathbf{d}_i} . \quad (5.33)$$

\mathbf{R}_{nn}^{-1} can be written as

$$\mathbf{R}_{nn}^{-1} = \sum_{n=1}^N \frac{1}{\lambda_n} \mathbf{v}_n \mathbf{v}_n^H \quad (5.34)$$

where λ_n and \mathbf{v}_n are the corresponding eigenvalues and eigenvectors of \mathbf{R}_{nn}^{-1} . The numerator in Eq. 5.32 is then

$$|\mathbf{d}_s^H \mathbf{R}_{nn}^{-1} \mathbf{d}_i|^2 = \left| \mathbf{d}_s^H \left[\sum_{n=1}^N \frac{1}{\lambda_n} \mathbf{v}_n \mathbf{v}_n^H \right] \mathbf{d}_i \right|^2 . \quad (5.35)$$

An analysis of the numerator shows that for the parameters used in the study of the previous section, it is the major contributing factor to the drop in sensitivity found at various interferer arrival angles. Figure 5.13 shows the numerator of ΔSNR as the interferer arrival angle changes. It is compared to the effective sensitivity as seen in Figure 5.10(a). The variation of the numerator of ΔSNR is the same as that of the effective sensitivity. A further look at the numerator shows that for the signal-to-interference ratio (SIR) region of interest here, $\mathbf{v}_n^H \mathbf{d}_i$ is the only term that varies greatly with different interferer arrival angles. It has two main contributors one of which occurs when \mathbf{v}_n is the eigenvector corresponding to the largest eigenvalue of \mathbf{R}_{nn}^{-1} , called \mathbf{v}_L or the principal eigenvector. The second major contributor is the eigenvector corresponding to the fourth largest eigenvalue. These two eigenvectors have a large weight corresponding to the center element, whereas the other eigenvectors have a very small weight at the center element. A plot of $\mathbf{v}_L^H \mathbf{d}_i$ as a function of arrival angle is seen in Figure 5.14. The angles where it is highest correspond to the angles where high effective sensitivity cannot be achieved.

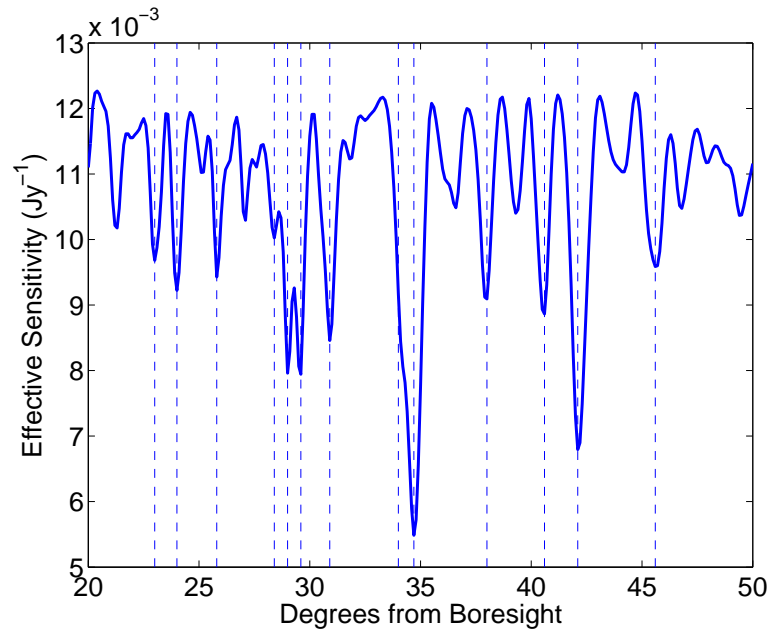
The dominant term in \mathbf{v}_L corresponds to the center element. This means that the largest contributor to $\mathbf{v}_L \mathbf{d}_i$ is due to $v_{L, \text{center element}}$ and $d_{i, \text{center element}}$. If the center element has a larger response in the direction of the interferer, $\mathbf{v}_L \mathbf{d}_i$ will be larger and sensitivity will drop. This is similar to the response of a signal at boresight. This can be seen by comparing \mathbf{d}_s and \mathbf{d}_i , the steering vectors corresponding to the signal of interest and the interferer respectively. The cosine of the angle between \mathbf{d}_s and \mathbf{d}_i was found. It is given as

$$\cos \psi = \frac{\mathbf{d}_s^H \mathbf{d}_i}{\|\mathbf{d}_s\|_2 \|\mathbf{d}_i\|_2} \quad (5.36)$$

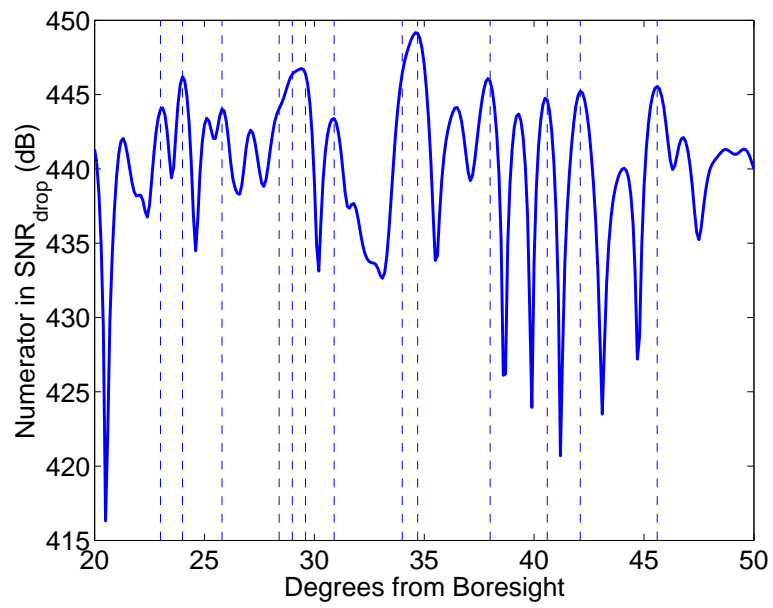
where ψ is the angle between \mathbf{d}_s and \mathbf{d}_i . The cosine of the angle between the vectors is high at angles where it is difficult to achieve high effective sensitivity. These results demonstrate that when the interferer appears as if it is arriving from boresight it is difficult to achieve high effective sensitivity. This is a similar effect to that which occurs at a grating lobe of an array.

As mentioned in Section 5.1, one outcome of having a large interferer response on the center element is that the outer elements must be weighted larger. This can be seen in Figure 5.16 which demonstrates that at angles where it is difficult to achieve high effective sensitivity the outer elements have larger weights. They are weighted larger in such a way that the interference is cancelled when the element signals are combined. This decreases the overall antenna gain and increases the spillover noise, thus reducing the effective sensitivity.

This analysis helps us understand why the effective sensitivity drops at certain interferer locations. Because these results are optimal, no better sensitivity can be obtained with this configuration of array elements. Other configurations were also implemented. Different element spacings were used, as were random perturbations in the locations of the array elements. The same phenomenon occurred for the different array configurations. For different configurations the drop in sensitivity would take place at different interferer locations. This problem could be minimized by using an even larger array or by using an auxiliary antenna in the RFI mitigation algorithm.



(a)



(b)

Figure 5.13: (a) The effective sensitivity of the 19-element array feed vs. interferer arrival angle using max SNR. (b) The numerator of ΔSNR as a function of interferer arrival angle.

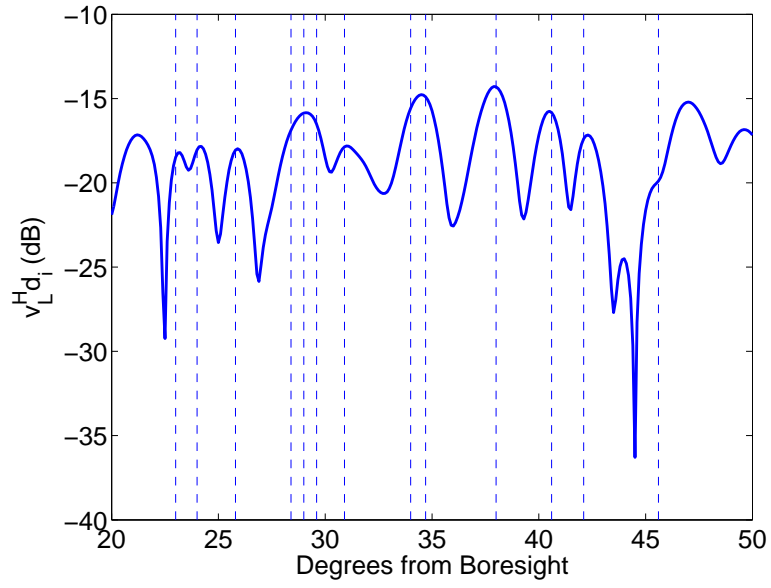


Figure 5.14: The quantity $\mathbf{v}_L^H \mathbf{d}_i$ as a function of interferer arrival angle.

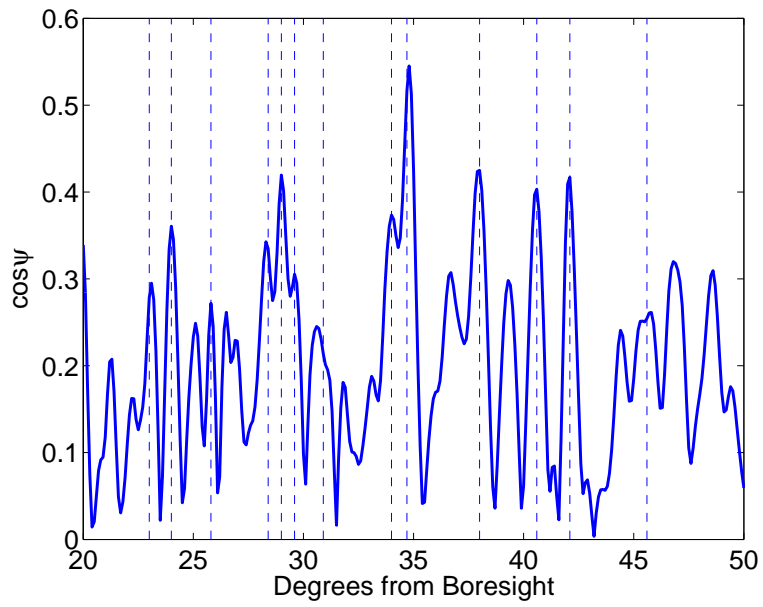


Figure 5.15: Comparison between \mathbf{d}_s and \mathbf{d}_i as a function of interferer arrival angle.

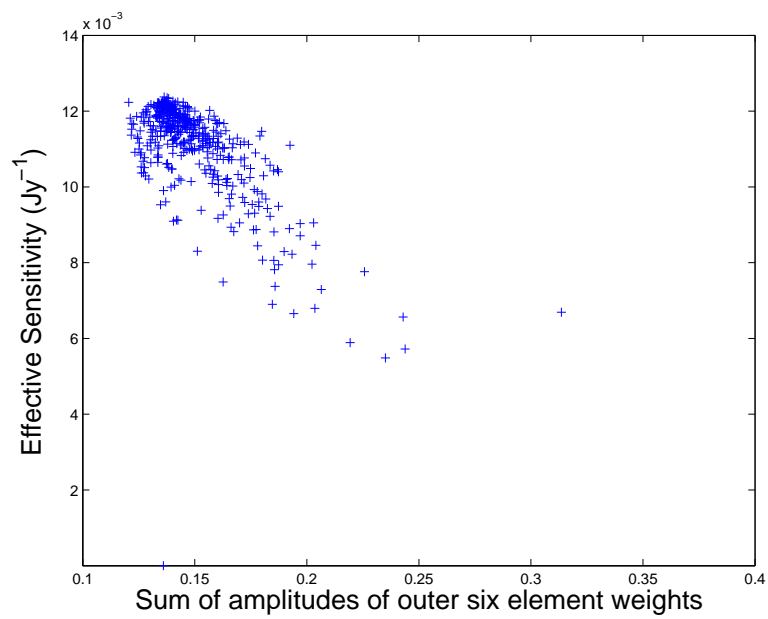


Figure 5.16: Effective sensitivity vs. sum of amplitudes of outer six element weights. When interferer power at the center element is large, outer element weights become large and sensitivity suffers.

Chapter 6

Conclusion

6.1 Contributions

The first contribution of this thesis entailed improving the RF receiver of the VSA platform. These improvements significantly reduced signals leaking through the system. A bandpass filter was designed and built which reduced the noise entering the receiver. These improvements enabled the observations of GLONASS satellites, different celestial sources, and the testing of adaptive algorithms.

The primary contribution of this thesis was the development and simulation of a phased array feed in conjunction with a reflector dish antenna. It was shown that a small 7-element array feed could produce a higher sensitivity than a standard waveguide feed, specifically 0.002 Jy^{-1} higher for a 25m reflector dish. This alone is motivation to pursue the future use of phased array feeds in radio astronomy. It was demonstrated that for a small array, the focal plane array provided a higher sensitivity than vertically displaced arrays. Beamscanning capabilities of a phased array were demonstrated. The main beam of a 7-element array could be steered to $.5^\circ$ with no loss in sensitivity. An example of simultaneously forming multiple high sensitivity beams was given. This would enable radio astronomers to do rapid sky surveys.

It was also shown for the first time that RFI mitigation was possible by using a phased array feed. It was shown that the effective sensitivity, where noise power is taken to be the sum of spillover and interference powers, can be comparable to

conventional sensitivity with no interference. Extensive simulation and analysis of interference mitigation possibilities were performed on both a 7-element and 19-element array feed. It was demonstrated that in principle a 19-element array feed could produce high sensitivity in the presence of a moving interferer. At some interferer arrival angles the sensitivity would drop, but not by more than 3 dB.

6.2 Future Work

There is still a great deal of research that needs to be performed on the phased array feed. More analysis on larger arrays needs to be done, along with analysis on the effects of different antenna elements, element spacing, and element locations. An analysis on the effects of mutual coupling on sensitivity also needs to be performed, as well as methods for coping with mutual coupling on such an array. Further development of different mitigation algorithms need to be performed, as well as the possibility of using an auxiliary antenna in conjunction with the phased array feed. And finally, a phased array feed needs to be constructed and tested on a radio astronomy platform so that real interference mitigation can take place.

APPENDIX

Appendix A

Single Feed Gain Pattern Computation Using GRASP8

For convenience GRASP8 uses normalized units for all of its electric and magnetic field computations. For an electric far field computation, the relation between the fields in the standard SI units and the units used in GRASP8 is given by

$$\mathbf{E}_{rad}^{SI} = \sqrt{2\eta} \frac{e^{-jkr}}{r} \mathbf{E}_{rad}^{GRASP8} . \quad (\text{A.1})$$

The electric field in SI units is V/m whereas the units used in GRASP8 are $\text{W}^{1/2}$. In GRASP8 the magnetic field normalized units are also $\text{W}^{1/2}$. By using these units all constants of nature are avoided in the field equations. This is convenient for GRASP8 where very large or small physical constants might give numerical problems.

GRASP8 also normalizes the electric and magnetic fields of each element such that the total radiated power of each element is 4π ,

$$P_{rad} = \int_0^{2\pi} \int_0^\pi \frac{|\mathbf{E}_{rad}^{SI}|^2}{2\eta} r^2 \sin\theta d\theta d\phi = 4\pi . \quad (\text{A.2})$$

Thus the output power pattern of a single element is actually the directivity pattern.

Directivity is defined as

$$D = \frac{|\mathbf{E}_{rad}^{SI}|^2 / 2\eta}{P_{rad} / 4\pi r^2} \quad (\text{A.3})$$

which leads to

$$D(\theta, \phi) = \frac{|\mathbf{E}_{rad}^{SI}(\theta, \phi)|^2 r^2}{2\eta} \quad (\text{A.4})$$

$$= |\mathbf{E}_{rad}^{GRASP8}(\theta, \phi)|^2 . \quad (\text{A.5})$$

In the case of a single antenna element plus a reflector dish the total radiated power is found by adding the scattered electric field \mathbf{E}_{scat}^{SI} with the incident electric field \mathbf{E}_{inc}^{SI}

from the feed element such that

$$P_{rad} = \int_0^{2\pi} \int_0^\pi \frac{|\mathbf{E}_{scat}^{SI} + \mathbf{E}_{inc}^{SI}|^2}{2\eta} r^2 \sin\theta d\theta d\phi = 4\pi . \quad (\text{A.6})$$

Since $P_{rad} = 4\pi$ the directivity pattern is found from Eq. A.3

$$D(\theta, \phi) = \frac{|\mathbf{E}_{scat}^{SI}(\theta, \phi) + \mathbf{E}_{inc}^{SI}(\theta, \phi)|^2}{2\eta} r^2 \quad (\text{A.7})$$

$$= |\mathbf{E}_{scat}^{GRASP8}(\theta, \phi) + \mathbf{E}_{inc}^{GRASP8}(\theta, \phi)|^2 . \quad (\text{A.8})$$

Appendix B

Spillover Noise Model

The following spillover noise model is used to find the correlation matrix R_{nn} used in the max SNR and LCMV algorithms. This model assumes the elements are isotropic radiators, and that the noise arrives at the elements from a warm background of 300 K. First, the model will be shown corresponding to a two dimensional case. Figure B.1.1 shows the case of M isotropic noise sources equally spaced around two isotropic receivers spaced a distance d apart. The noise sources are assumed to be in the far field of the receivers. The received signals are

$$x_1(t) = \sum_{m=1}^M x_m(t) \quad (\text{B.1})$$

$$x_2(t) = \sum_{m=1}^M x_m(t) e^{-jkd \cos \phi_m} . \quad (\text{B.2})$$

The correlation between the two receivers can be found from

$$\mathbf{R}(d) = \left\langle \sum_1^M x_m^*(t) \cdot \sum_1^M x_p(t) e^{-jkd \cos \phi_p} \right\rangle \quad (\text{B.3})$$

$$= \sum_1^M \sum_1^M \langle x_m^*(t) x_p(t) \rangle e^{-jkd \cos \phi_p} \quad (\text{B.4})$$

$$= \sum_1^M \sum_1^M \langle x_m^*(t) x_m(t) \rangle \delta_{mp} e^{-jkd \cos \phi_p} \quad (\text{B.5})$$

$$= \sum_1^M \langle x_m^*(t) x_m(t) \rangle e^{-jkd \cos \phi_m} \quad (\text{B.6})$$

$$= \frac{\sigma^2}{M} \sum_1^M e^{-jkd \cos \phi_m} . \quad (\text{B.7})$$

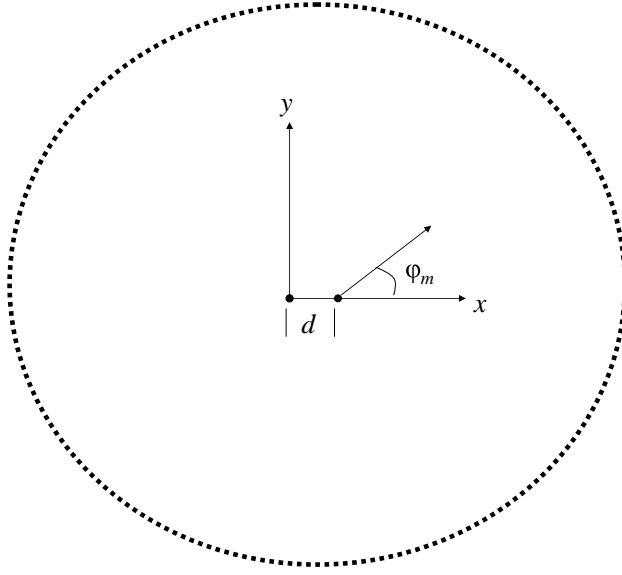


Figure B.1: Two isotropic radiators separated by a distance d and surrounded by M noise sources.

This can be rewritten as

$$\mathbf{R}(d) = \frac{\sigma^2}{2\pi} \sum_1^M \frac{2\pi}{M} e^{-jkd \cos \phi_m} . \quad (\text{B.8})$$

If we let $M \rightarrow \infty$ then this is the Riemann sum for an integral over ϕ ,

$$\lim_{M \rightarrow \infty} \sum_1^M \frac{2\pi}{M} e^{-jkd \cos \phi_m} = \int_0^{2\pi} d\phi e^{-jkd \cos \phi}$$

and thus

$$\mathbf{R}(d) = \frac{\sigma^2}{2\pi} \int_0^{2\pi} d\phi e^{-jkd \cos \phi} \quad (\text{B.9})$$

which evaluates to

$$\mathbf{R}(d) = \sigma^2 J_0(kd) . \quad (\text{B.10})$$

In three dimensions, the equivalent setup would be a sphere of noise sources surrounding the receivers. The phase change from receiver to receiver now has a θ component and the integral is now over a sphere instead of a circle. Thus for a sphere

of noise sources,

$$\mathbf{R}(d) = \frac{\sigma^2}{4\pi} \int_0^{2\pi} \int_0^\pi e^{-jkd \sin \theta \cos \phi} \sin \theta d\theta d\phi \quad (\text{B.11})$$

$$= \frac{\sigma^2}{4\pi} \int_0^\pi 2\pi J_0(kd \sin \theta) \sin \theta d\theta \quad (\text{B.12})$$

$$= \frac{\sigma^2}{4\pi} (2\pi) \left(2 \frac{\sin(kd)}{kd} \right) \quad (\text{B.13})$$

$$= \sigma^2 \frac{\sin(kd)}{kd} . \quad (\text{B.14})$$

Now to find $\mathbf{R}_{nm}(d)$ for an array feed, a more general three dimensional solution is used,

$$\mathbf{R}(d) = \frac{\sigma^2}{\Omega_{tot}} \int_{\Omega_{tot}} d\Omega e^{-jkd \sin \theta \cos \phi} \quad (\text{B.15})$$

where Ω_{tot} is the total solid angle from which the array receives power from the noise sources. The integral takes place for all ϕ and for θ only from the edge of the dish to the lateral plane of the array as in Figure B.2.2. $\mathbf{R}(d)$ becomes

$$\mathbf{R}(d) = \frac{\sigma^2}{\Omega_{tot}} \int_0^{2\pi} \int_{\theta_0}^{\pi/2} e^{-jkd \sin \theta \cos \phi} \sin \theta d\theta d\phi \quad (\text{B.16})$$

$$= \frac{2\pi\sigma^2}{\Omega_{tot}} \int_{\theta_0}^{\pi/2} J_0(kd \sin \theta) \sin \theta d\theta \quad (\text{B.17})$$

$$(\text{B.18})$$

where

$$\Omega_{tot} = \int_0^{2\pi} \int_{\theta_0}^{\pi/2} \sin \theta d\theta d\phi . \quad (\text{B.19})$$

For the reflector considered in this thesis, $\theta_0 = 69.5^\circ$ and σ^2 is the total noise power received by a single element,

$$\sigma^2 (\text{W/Hz}) = k_B T_B \frac{\Omega_{tot}}{\Omega_{Max}} \quad (\text{B.20})$$

where $k_B = 1.38 \times 10^{-23} (\text{J/K})$, $T_B = 300 \text{ K}$, and

$$\Omega_{Max} = \int_0^{2\pi} \int_0^\pi \sin \theta d\theta d\phi = 4\pi . \quad (\text{B.21})$$

To include the noise due to the LNA a diagonal term is added to the noise matrix \mathbf{R}_{nm} . This term is the noise power at each channel due to the LNA. It is found from

$$\sigma_{LNA}^2 = k_B T_{LNA} . \quad (\text{B.22})$$

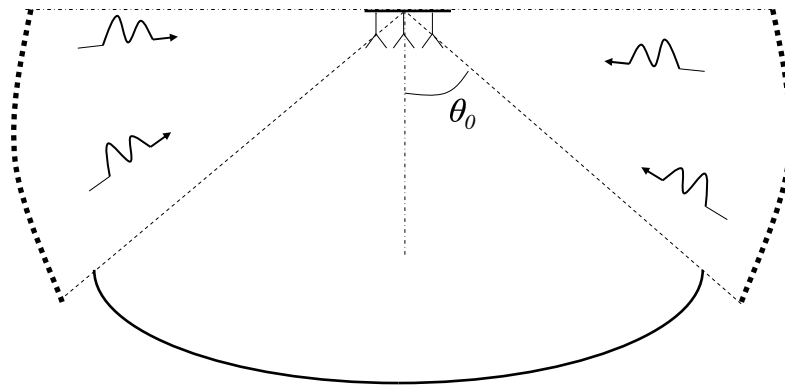


Figure B.2: Power from noise sources collected by the phased array feed.

For all of the simulations given in this thesis a LNA noise temperature of 15 K was used.

Bibliography

- [1] C. Barnbaum and R. F. Bradley, “A new approach to interference excision in radio astronomy: Real-time adaptive cancellation”, in *Astronomical Journal*, November 1998, vol. 116, pp. 2598–2614.
- [2] J. R. Fisher, “Techniques for Coping with RFI”, in *NRAO Papers*, August 1999.
- [3] J. R. Fisher, “RFI and How to Deal with It”, in *NRAO Papers*, June 2001.
- [4] R. A. Perley, “Attenuation of rfi by interferometric imaging arrays”, in *Proceedings of the IEEE APS-URSI Symposium*, June 2003.
- [5] W. A. Baan, P. A. Fridman, and R. P. Millenaar, “Rfi mitigation at wsrt: algoritihms, test observations, system implementation”, in *Proceedings of the URSI General Assembly XXVII*, August 2002.
- [6] S. W. Ellingson, J. D. Bunton, and J. F. Bell, “Removal of the GLONASS C/A Signal from OH Spectral Line Observations using a Parametric Modelling Technique”, in *The Astrophysical Journal Supplement Series*, July 2001, number 135, pp. 87–93.
- [7] G. C. Bower, “A radio frequency interference mitigation strategy for the allen telescope array”, in *Proceedings of the URSI General Assembly XXVII*, August 2002.
- [8] J. F. Bell, P. J. Hall, R. J. Sault, and L. Kewley, “Implementing Interference Suppression: Impacts on SKA System Design”, in *Technological Pathways to the SKA*, August 2000.

- [9] L. Li, B. D. Jeffs, A. J. Poulsen, and K. F. Warnick, “Analysis of Adaptive Array Algorithm Performance for Satellite Interference Cancellation in Radio Astronomy”, in *URSI General Assembly XXVII*. Nat. Academies of Sciences and Engineering, August 2002, Maastricht the Netherlands.
- [10] B. D. Jeffs, K. F. Warnick, and L. Li, “Improved Interference Cancellation in Synthesis Array Radio Imaging Using Auxiliary Antennas”, in *IEEE International Conference on Acoustics, Speech, and Signal Processing*, April 2003, Hong Kong.
- [11] B. D. Jeffs, L. Li, and K. F. Warnick, “Auxiliary Antenna Assisted Interference Cancellation for Radio Astronomy Imaging Arrays”, in *IEEE Transactions on Signal Processing*, February 2003, in review.
- [12] A. J. Poulsen, “Real-time Adaptive Cancellation of Satellite Interference in Radio Astronomy”, Master’s thesis, Brigham Young University, August 2003.
- [13] A. J. Poulsen, B. D. Jeffs, C. K. Hansen, K. F. Warnick, and J. R. Fisher, “Real-Time Adaptive Cancellation of GLONASS Interference in OH Signal Observations at the Green Bank Telescope”, in *Proceedings of the URSI North American Radio Science Meeting*, June 2003.
- [14] “Small Radio Telescope (SRT)”, <http://web.haystack.mit.edu/SRT/>, January 2003.
- [15] B. T. Walkenhorst, “Development of a Radio Telescope Receiver for Research in Radio Frequency Interference Mitigation”, Master’s thesis, Brigham Young University, August 2001.
- [16] D. M. Pozar, *Microwave Engineering*, John Wiley & Sons, Inc., second edition, 1998.
- [17] M. Gillick, I. D. Robertson, and J. S. Joshi, “Direct Analytical Solution for the Electric Field Distribution at the Conductor Surfaces of Coplanar Waveguides”,

- in *IEEE Transactions on Microwave Theory and Techniques*, 1993, vol. 41, pp. 129–135.
- [18] S. W. Lee and M. L. Zimmerman, “Reflector spillover loss of an open-ended rectangular and circular waveguide feed”, in *IEEE Transactions on Antennas and Propagation*, June 1990, vol. 38, pp. 940–942.
- [19] P. Shelton, “Multiple-feed systems for objectives”, in *IEEE Transactions on Antennas and Propagation*, November 1965, vol. 13, pp. 992–994.
- [20] S. J. Blank and W. A. Imbriale, “Array feed synthesis for correction of reflector distortion and vernier beamsteering”, in *IEEE Transactions on Antennas and Propagation*, October 1988, vol. AP-36.
- [21] J. R. Fisher, “Phased array feeds for low noise reflector antennas”, in *NRAO Electronics Division Internal Report*, September 1996, number 307.
- [22] K. Woo, “Multiple beam antenna feed development”, in *IEEE Antennas and Propagation Society International Symposium Digest*, June 1986, pp. 409–412.
- [23] M. S. Reid and D. A. Bathker, “Low Noise Microwave Receiving Systems on a 64 m Antenna”, in *Microwave Symposium Digest, GMTT International*, May 1972, vol. 72, pp. 17–20.
- [24] J. Huang and V. Jamnejad, “A microstrip array feed for land mobile satellite reflector antennas”, in *IEEE Transactions on Antennas and Propagation*, February 1989, vol. 37, pp. 153–158.
- [25] A. K. Singh and G. Kumar, “EMCP microstrip antennas as feed for satellite receiver”, in *IEEE Antennas and Propagation Society International Symposium Digest*, July 1996, vol. 2, pp. 1274–1277.
- [26] W. J. Hall, P. C. Wilcockson, M. H. Skeen, S. J. Stirland, L. Hilliard, H. S. Ghuman, and L. E. Comtesse, “Satellite antenna subsystem using shaped reflector and multiple feed gridded reflectors”, in *IEEE Antennas and Propagation Society International Symposium Digest*, April 1989, vol. 1, pp. 60–64.

- [27] R. A. Perrott and J. M. Griffin, “L-band antenna systems design”, in *IEEE Colloquium on INMARSAT-3*, November 1991.
- [28] D. Emerson and J. Payne, Eds., *Astronomical Society of the Pacific Conference Series, Multi-Feed Systems for Radio Telescopes.*, vol. 75, San Francisco: Astronomical Society of the Pacific, 1995.
- [29] B. Gaensler, N. McClure-Griffths, J. Dickey, and A. Green, “The southern galactic plane survey, new views of the deep south”, in *Proceedings of the URSI General Assembly XXVII*, August 2002.
- [30] “The parkes multibeam receiver”, <http://www.atnf.csiro.au/research/multibeam/.overview.html>, January 2004.
- [31] J. Karimi and S. Blostein, “Parabolic reflector array signal processing for improved rural area coverage in personal satellite communications”, in *1996 5th IEEE International Conference on Universal Personal Communications*, September 1996, vol. 1.
- [32] J. Karimi and S. D. Blostein, “Parabolic reflector array signal processing for improved rural area coverage in personal satellite communications”, in *5th IEEE International Conference on Universal Personal Communications*, September 1996, vol. 1, pp. 453–457.
- [33] C. Dau-Chyrh, H. Chang-Nan, H. Chia-I, and H. Ko-Tai, “Pattern synthesis of the offset reflector antenna system with less complicated phased array feed”, in *IEEE Transactions on Antennas and Propagation*, February 1994, vol. 42, pp. 240–245.
- [34] K. Hariu, H. Tsunoda, Y. Kawakami, and T. Noguchi, “Pattern correction in large deployable reflector antennas with phased array feed”, in *IEEE Antennas and Propagation Society International Symposium Digest*, July 1997, vol. 2, pp. 844–847.

- [35] A. Mrstik and P. Smith, “Scanning capabilities of large parabolic cylinder reflector antennas with phased-array feeds”, in *IEEE Transactions on Antennas and Propagation*, May 1981, vol. 29, pp. 455–462.
- [36] S. H. Huynh, A. Ho, and C. H. Chen, “A septet beam forming network for reflector multiple-beam antennas”, in *IEEE Antennas and Propagation Society International Symposium Digest*, July 1997, vol. 2, pp. 1394–1397.
- [37] J. R. Fisher and R. F. Bradley, “Technical progress on array feeds and RFI cancellation”, in *International Square-Kilometer Array Science Meeting*. July 1998, Calgary, Canada.
- [38] J. R. Fisher, R. F. Bradley, R. Escoffer, and K. Saini, “Phased array feed design and prototype”, in *Proceedings of the URSI General Assembly*. August 1996, Lille, France.
- [39] R. F. Bradley, K. Saini, and J. R. Fisher, “A prototype array feed - design and construction”, in *USNC/URSI Meeting*. January 1996, Boulder, Colorado.
- [40] J. R. Fisher and R. F. Bradley, “Full sampling array feeds for radio telescopes”, in *Proceedings of the SPIE, Radio Telescopes*, 2000, vol. 4015, pp. 308–318.
- [41] “The 19-element feed array at nrao”, <http://www.gb.nrao.edu/gbt/bfa/>, January 2004.
- [42] Mini-Circuits, “Improved ERA Amplifiers (AN-60-010)”, July 2001.
- [43] J. A. Kong, *Electromagnetic Wave Theory*, EMW Publishing, 2000.
- [44] J. R. Fisher, “Phased array feeds for low noise reflector antennas”, in *NRAO Electronics Division Internal Report*, September 1996, number 307.
- [45] J. R. Fisher and R. F. Bradley, “Full-Sampling Focal Plane Arrays”, in *NRAO Electronics Division Internal Report*, December 1999.

- [46] P. T. Lam, S. Lee, D. C. Chang, and K. C. Lang, “Directivity Optimization of a Reflector Antenna with Cluster Feeds: A Closed-Form Solution”, in *IEEE Transactions on Antennas and Propagation*, November 1985, vol. AP-33.
- [47] W. L. Stutzman, *Antenna theory and design*, John Wiley & Sons, Inc., second edition, 1998.
- [48] B. D. Van Veen and K. M. Buckley, “Beamforming: A Versatile Approach to Spatial Filtering”, in *IEEE ASSP Magazine*, April 1988.